ΠΑΝΕΠΙΣΤΗΜΙΟ ΚΡΗΤΗΣ
ΔΙΑΤΜΗΜΑΤΙΚΟ ΜΕΤΑΠΤΥΧΙΑΚΟ
ΠΡΟΓΡΑΜΜΑ ΣΠΟΥΔΩΝ
**ΟΠΤΙΚΗ & ΟΡΑΣΗ**

# ΜΕΤΑΠΤΥΧΙΑΚΗ ΕΡΓΑΣΙΑ

## «*Optical resolution photoacoustic microscopy for the quantitative analysis of contact lenses*»

**Μαργαρίτα Τσαγκαράκη**

**Ηράκλειο 2017**

This thesis was completed under the scientific supervision of:

- Dr. Sotiris Plainis
- Dr. George J. Tserevelakis
- Dr. Giannis Zacharakis

➢ The examination committee was consisted of the following members:

- Prof. Miltiadis Tsilimbaris
- Prof. Michael I. Taroudakis
- Prof. Dimitris Papazoglou

## Table of Contents

# *Ευχαριστίες*

Η παρούσα εργασία εκπονήθηκε στα πλαίσια του διατμηματικού μεταπτυχιακού προγράμματος σπουδών "Οπτική & Όραση" σε συνεργασία με το Ινστιτούτο Οπτικής και Όρασης του Τμήμα Ιατρικής στο Πανεπιστήμιο Κρήτης, καθώς και το εργαστήριο in-vivo απεικόνισης του Ινστιτούτου Ηλεκτρονικής Δομής και Λέιζερ (ΙΗΔΛ-IESL) του Ιδρύματος Τεχνολογίας και Έρευνας (ITE-FORTH).

Θα ήθελα αρχικά να ευχαριστήσω την συμβουλευτική επιτροπή της εργασίας που μου έδωσε την ευκαιρία να ασχοληθώ με την έρευνα σε ένα εξαιρετικά καινοτόμο και ενδιαφέρων τομέα που συνδυάζει την οπτοακουστική μικροσκοπία με το πεδίο της οπτομετρίας, και έχει τη δυναμική να οδηγήσει σε αξιόλογα αποτελέσματα. Πιο συγκεκριμένα, ευχαριστώ θερμά τον Δρ. Γιάννη Ζαχαράκη, ερευνητή Β' του ΙΗΔΛ και υπεύθυνο του εργαστηρίου in-vivo απεικόνισης, για την άψογη συνεργασία και καθοδήγηση. Ευχαριστω επίσης, τον Δρ. Σωτήρη Πλαΐνη, καθηγητή του προγράμματος "Οπτική & 'Οραση" στον οποίο ανήκει και η αρχική ιδέα της παρούσας εργασίας. Ο κ. Πλαΐνης, καθ' όλη τη διάρκεια της ερευνητικής μου προσπάθειας προσέφερε τις εξειδικευμένες γνώσεις του στον τομέα της οπτομετρίας, ενώ παράλληλα παρείχε όλους τους φακούς επαφής που χρησιμοποιήθηκαν στην πειραματική διαδικασία.

Ένα μεγάλο ευχαριστώ στο Δρ. Γεώργιο Τσερεβελάκη για την εμπιστοσύνη, την υποστήριξη την συνεχή καθοδήγηση και επίβλεψη, δημιουργώντας με αυτόν τον τρόπο ένα ιδανικό περιβάλλον για την απόκτηση γνώσεων και εργαστηριακής εμπειρίας στον τομέα της οπτοακουστικής μικροσκοπίας.

Να ευχαριστήσω επίσης τον Καθ. Μιλτιάδη Τσιλιμπάρη, η συμβολή του οποίου υπήρξε καθοριστική στην εξέλιξη της εργασίας μέσω των γόνιμων συζητήσεων και συμβουλών του.

Τέλος, να ευχαριστήσω όλα τα μέλη του εργαστηρίου in-vivo απεικόνισης για την άψογη συνεργασία, και ειδικά την κα Στέλλα Αβτζή που συνεισέφερε στην πειραματική διαδικασία με την κατασκευή της απαραίτητης βάσης τοποθέτησης των φακών επαφής.

# *Περίληψη*

Η καθημερινή χρήση Φακών Επαφής (ΦΕ) είναι ευρέως διαδεδομένη και οδηγεί στην κατασκευή ενός τεράστιου αριθμού ΦΕ ετησίως. Επομένως, είναι αναγκαίο να αναπτυχθεί μια τεχνική ποσοτικής αλλά και ποιοτικής αξιολόγησης των ΦΕ. Για την σωστή και ολοκληρωμένη εκτίμηση των ΦΕ σε βιομηχανική κλίμακα, πρέπει να ληφθούν υπ'όψη ορισμένες παράμετροι, όπως οι οπτικές/γεωμετρικές ιδιότητες, η εφαρμογή στην επιφάνεια του κερατοειδούς, τα υλικά κατασκευής, ο βαθμός διαπερατότητας στο οξυγόνο κτλ. Η τεχνική αξιολόγησης πέρα από ακρίβεια, ορθότητα και επαναληψιμότητα είναι σημαντικό να διαθέτει ευκολία και ταχύτητα εφαρμογής, καθώς και ένα σχετικά μικρό κόστος.

Στα πλαίσια της παρούσας μεταπτυχιακής εργασίας, παρουσιάζεται μια νέα μεθοδολογία χαρακτηρισμού των γεωμετρικών και οπτικών ιδιοτήτων ΦΕ, η οποία βασίζεται στην φωτοακουστική μικροσκοπία οπτικής ανάλυσης (Optical Resolution Photoacoustic Microscopy, OR-PAM). Η απεικόνιση μέσω της OR-PAM επιτυγχάνεται μέσω της ανίχνευσης των ακουστικών κυμάτων που παράγονται σε ένα υλικό μέσο, έπειτα από την οπτική απορρόφηση ακτινοβολίας η οποία εκπέμπεται από μια παλμική ή διαμορφούμενης ισχύος πηγή λέιζερ. Παρά το γεγονός ότι η OR-PAM έως τώρα έχει εφαρμοστεί αποκλειστικά σε βιολογικά δείγματα, αποδεικνύουμε πως έχει τη δυναμική να απεικονίσει την πρόσθια και οπίσθια επιφάνεια ενός ΦΕ, έπειτα από την αντίστοιχη επίστρωσή τους με λεπτά στρώματα χρωστικών ουσιών, τα οποία χαρακτηρίζονται από διαφορετικές ιδιότητες οπτικής απορρόφησης. Πιο συγκεκριμένα, για την επίστρωση της πρόσθιας επιφάνειας του ΦΕ, χρησιμοποιήθηκε μαύρο μελάνι με υψηλή οπτική απορρόφηση τόσο στο κοντινό υπέρυθρο όσο και στα ορατά μήκη κύματος. Αντίθετα, η οπίσθια επιφάνεια καλύφθηκε με κόκκινο μελάνι αμελητέας απορρόφησης στο κοντινό υπέρυθρο και υψηλής απορρόφησης ιδιαίτερα στην περιοχή των μηκών κύματος που αντιστοιχεί στο πράσινο. Χρησιμοποιώντας έτσι δύο μήκη κύματος (1064 και 532 nm) επιτεύχθηκε η διαδοχική απεικόνιση των επιφανειών, ενώ από το γινόμενο της χρονικής διαφοράς στα ακουστικά σήματα που παράχθηκαν στο κέντρο τους με την ταχύτητα του ήχου, υπολογίστηκε το κεντρικό πάχος του ΦΕ. Προσαρμόζοντας δευτεροβάθμια πολυώνυμα στις υπολογισμένες επιφάνειες, εξάχθηκαν οι χάρτες τοπικής ακτίνας καμπυλότητας και διοπτρικής δύναμης, οι οποίοι μας επέτρεψαν τον υπολογισμό της ολικής δύναμης του υπό μελέτη ΦΕ.

Για την κατάδειξη της προτεινόμενης μεθοδολογίας ως ενός ισχυρού εργαλείου μετρολογίας αλλά και ποιοτικής εξέτασης ΦΕ, χρησιμοποιήθηκε μια ποικιλία φακών όπως κοσμητικοί φακοί αλλαγής χρώματος, βιομηχανικά βαμμένοι φακοί για περιπτώσεις ανιριδίας, μαλακοί φακοί, καθώς και ημίσκληροι φακοί. Στην τελευταία περίπτωση, τα αποτελέσματα των μετρήσεων μέσω OR-PAM συγκρίθηκαν με τις τιμές που δίνονται από τον κατασκευαστή, από όπου διαπιστώθηκε υψηλή συμφωνία στις γεωμετρικές αλλά και οπτικές παραμέτρους των ΦΕ, αποδεικνύοντας την αξιοπιστία της συγκεκριμένης προσέγγισης.

Συμπερασματικά, η ευκολία ανάπτυξης ενός τέτοιου απεικονιστικού συστήματος, σε συνδυασμό με την αξιοπιστία και το χαμηλό κόστος της μεθοδολογίας που ακολουθήθηκε, την καθιστούν κατάλληλη για μια ευρεία εφαρμογή σε βιομηχανική κλίμακα όσον αφορά τον ποιοτικό έλεγχο και τη βελτιστοποίηση των ιδιοτήτων ΦΕ.

# *Abstract*

The daily use of Contact Lenses (CL) is widely spread, and leads to the production of a huge number of CLs every year. Therefore, the need for the development of techniques being able to characterize CLs' parameters both qualitatively and quantitatively is huge. In order to have an accurate and comprehensive evaluation of CLs at industrial level, several parameters have to be taken into account such as lens fitting, material hydration, oxygen permeability, edge fitting, etc. Besides precision, accuracy and repeatability, this new technique should be easy to use, relatively fast and with low cost.

In the context of this master thesis, a novel characterization methodology of CLs geometrical and optical properties is presented, based on Optical Resolution Photoacoustic Microscopy (OR-PAM). The OR-PAM imaging is achieved through the detection of the acoustic waves generated in a medium, following the absorption of irradiation emitted by a pulsed or intensity-modulated laser source. Despite the fact that OR-PAM has been employed so far exclusively on biological specimens, we demonstrate that it has the potential to reconstruct both the anterior and posterior surface of a CL, after their respective coating with thin pigmented layers, characterized by different optical absorption properties. More specifically, for the coating of the anterior surface, we used black ink with high absorption at both the near infrared and the visible wavelengths. On the contrary, the posterior surface was covered with red ink of negligible absorption in the near infrared; however of high absorption, mainly in the green spectral region. With the use of two optical wavelengths (1064 and 532 nm), the sequential imaging of the CL's surfaces was achieved, whereas from the product of the temporal difference for the acoustic signals generated at the CL center with the speed of sound, we estimated the respective central thickness. By fitting a second order polynomial to the calculated surfaces, the maps of local radius of curvature and dioptric power were extracted, allowing for the determination of the CL's total power.

For the demonstration of the proposed methodology as a powerful metrology, as well as, a qualitative inspection tool, a large variety of CLs was used such as cosmetic lenses, industrially colored lenses for aniridia cases, soft CLs and semi-rigid CLs. For the latter case, the obtained results through OR-PAM were compared to the values provided by the manufacturer, to show an excellent agreement for the geometrical and optical parameters measured, proving thus the reliability of our approach.

In conclusion, the implementation simplicity of such an imaging system, in combination to the reliability and the low cost of the followed methodology, render it suitable for broad industrial application concerning the quality inspection and optimization of CLs parameters.

# *Chapter 1: Imaging and metrology methods for the characterization of contact lenses*

A huge number of Contact lenses is manufactured each year. Thus, there is great need of a testing technique for qualitative and quantitative inspection of Cls. Multiple aspects of Cls' function/behavior should be taken into account, such as lens fitting, material hydration, oxygen permeability, edge fitting, etc in order to evaluate them correctly.

Besides precision, accuracy and repeatability this new technique should be easy to use, relatively fast and not destructive. This justifies the fact that imaging and metrology of Cls is a field of intense ongoing research, with a significant number of proposed techniques.

## *1.1 Interferometry*

Interferometry is an important investigation technique in the field of optical metrology. As a non-invasive and non-contact method, it has been widely used for the evaluation of contact lenses' (Cl) surface curvature, thickness variation, dioptric power and edge fitting of the contact lens (El-Nashar et al.,1979; Achatz et al., 1983; Plakitsi et al.).

A Linnic microinterferometer is an instrument based on the Michelson interferometry is shown in figure 1.1( El-Nashar et al.,1979). The source *S* is a monochromatic light divided by a beam splitter prism $P_1$. The first light wave after passing through parallel plate $G_2$ and the objective $O_2$, is reflected by the Cl, *P* placed in saline. The second one propagates through the prism $P_1$ and the parallel plates $G_1$ and $O_1$ in order to be reflected by the comparison mirror *SV*. The two waves recombine at the splitting prism $P_1$, creating interference fringes that are photographed. The percentage of the reflected light from a surface is given by the expression

$$K = \left( \frac{N_2 - N_1}{N_2 + N_1} \right) \quad (1.1)$$

where K is the reflection factor and $N_1$ and $N_2$ are the refractive indices. So, for a Cl immersed in water the reflectance from the interface is around 12%.

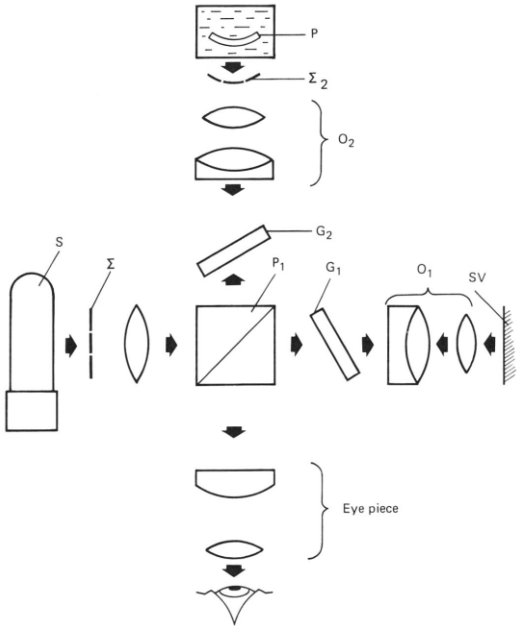


***Fig. 1.1:*** *Principle of the Linnik microinterferometer*

Interferometry is a sensitive method with quick signal recording. However, it has disadvantages such as high cost, complex apparatus that is the reason why it is relatively difficult to use (tedious alignment, sensitive to vibration, requires isolation).

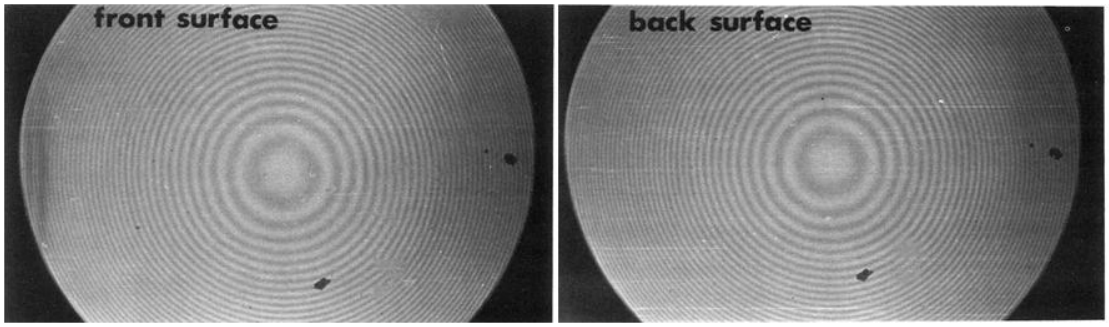


***Fig. 1.2:*** *Interferogram of the front and back surface of a -2.00 D soft contact lens*

Interferometry can be combined with other techniques. There are instruments incorporating a Shack-Hartmann wavefront sensor (SHWS), a machine vision sensor and a low coherence interferometer (LCI), all coaxially aligned. SHWS measures power, spherical, cylinder prism and higher order wavefront aberrations. The vision sensor measures the diameter and locates the center of the lens. LCI calculates center thickness sagittal depth and index of refraction of the contact lens (Marcus M.A. et al 2015).

## *1.2 Optical Coherence Tomography*

Optical Coherence Tomography (OCT) is used as a medical imaging modality for optical scattering media and optically transparent (e.g. cornea imaging). OCT has been successfully applied in ophthalmology and optometry because it can provide 3D images at a spatial resolution in the order of several hundreds of nanometers within the retina; The OCT technique is based on low-coherence interferometry, employing near-infrared light. Scanning the light beam on the sample enables non-invasive cross-sectional imaging up to 4mm in depth for optically transparent specimens. A typical single point OCT setup as shown in Figure 1.3, consists of an interferometer and a low coherence, broad bandwidth laser source.

The laser beam in an OCT system, similarly to interferometry, is divided by a beam splitter into two parts. The first light wave is reflected by a mirror in order to be used as reference light. The second one propagates in order to be reflected by the sample under investigation. The interference pattern is produced by these two light waves, only when both them have travelled the same optical distance.

For a time domain OCT, a reflectivity profile of the sample is created by scanning the reference mirror. Areas of the sample that reflect back a lot of light will create greater interference than areas that don't. Any light that is outside the short coherence length will not interfere. This reflectivity profile, called an A-scan, contains information about the spatial dimensions and location of structures within the item of interest. A cross-sectional tomograph (B-scan) may be achieved by laterally combining a series of these axial depth scans (A-scan).

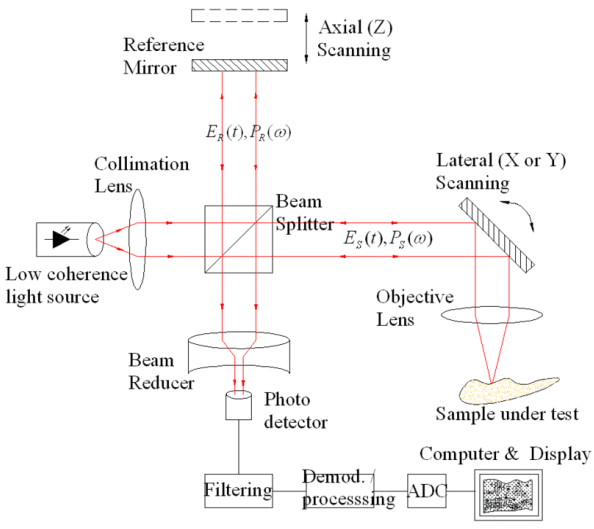


***Fig. 1.3:*** *Typical optical setup of single point OCT (*CC-BY-SA-2.5. https://en.wikipedia.org/wiki/Optical_coherence_tomography#/media/File:OCT_B-Scan_Setup.GIF)

During the past few years, OCT has been employed in CL practice, to measure several optical and geometrical parameters, as well as for the investigation of lens fitting on the cornea.. A major advantage of OCT is that it can be performed in vivo, in contact lens wearers, since it is a non-invasive and non-contact method. Thus, the resulting 3D images can provide valuable information about the CL fitting on the ocular surface, the lens edge fitting and the thickness of the tear film (Rodrigues P. et al. 2015; Shen M. et al. 2011; Kaluzny B.J. 2006; Kaluzny B.J. 2007 ). Concerning CLs metrology, there are many studies demonstrating the feasibility of OCT systems to evaluate the entire thickness profiles of CLs in vivo and in vitro (Davidson B.R. et al. 2010; Tao A. et al 2013)

Figure 1.4 depicts an OCT cross sectional image of a toric CL in saline solution (A) and in vivo (D) and their segmented surfaces, anterior with red color and posterior with green color can be seen in (B) and (E) respectively . (C) is the thickness map of the toric lens which is the same in vivo and in vitro.

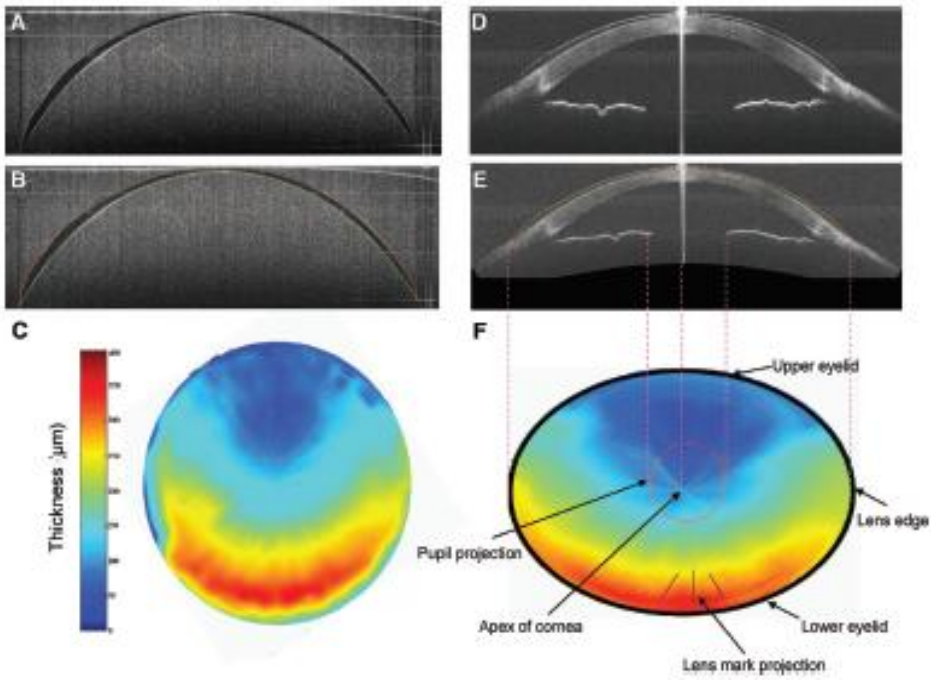


***Fig. 1.4:*** *Imaging entire CL in vitro and on the eye with a Spectral Domain OCT: (A) Cross-sectional OCT image of a toric soft contact lens immersed in saline; Scan width 15.6mm. (B) The segmented surfaces of the CL from figure 1.4(A). Red curve: anterior surface of the lens. Green curve: posterior surface of the lens. (C) Thickness map of the soft CL in vitro. (D) Cross-sectional OCT image of a toric soft lens on a healthy eye acquired in horizontal meridian. A scan width of 20mm was applied for three-dimensional raster scan. (E) The segmented surfaces of the contact lens from figure 1.4 (D). (F) Thickness map of lens on the eye. The resolution is ~6,0µm axially and ~15 µm transversally (*Shen M. et al. 2011)

The topographic analysis shown below is of a toric soft lens placed in a wet cell. By generating the 3D reconstruction of the lens, the parameters determined were lens thickness and radius of curvature for both surfaces using the best fit spherical surfaces. The power of the lens was calculated using the thick lens equation

$$P = (n-1)\left[\frac{1}{R_1} + \frac{1}{R_2} - \frac{(n-1)*CT}{n*R_1*R_2}\right] \quad (1.2)$$

The quantitative topographic results show good repeatability and match the manufactures specification (Karnowski K. et al, 2014).

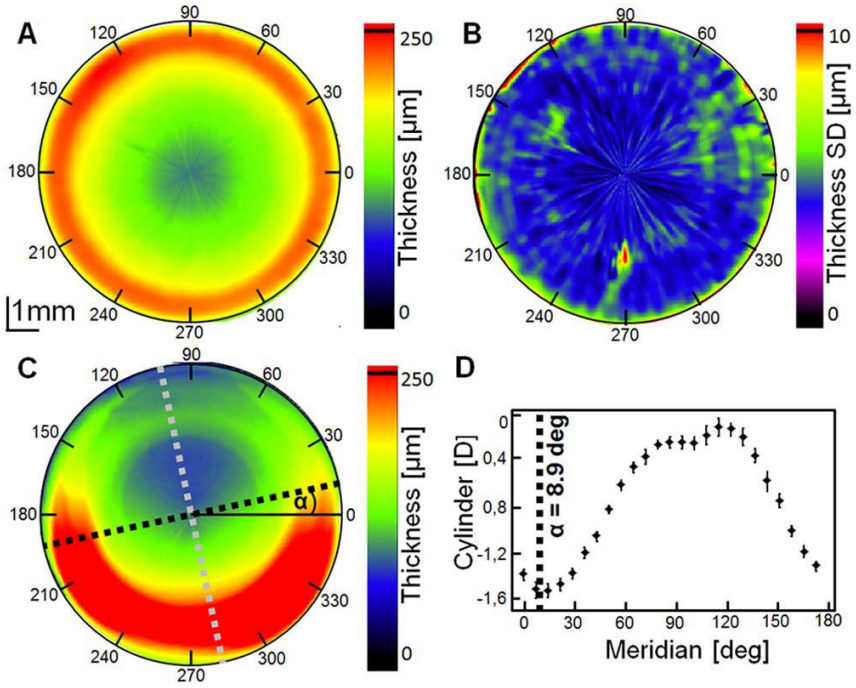


***Fig. 1.5:*** *Quantitative CL evaluation with a swept source OCT . (A) Averaged thickness map and (B) standard deviation map of the thickness calculated from 10 measurements of the spherical soft CL. (C) Thickness map of the toric soft CL with clearly visible bottom weighting ballast with the axis rotated by 8.9 deg . (D) Astigmatism of the toric soft CL. The system's resolution is 9µm axially in air and 24.8 transversally* (Karnowski K. et al, 2014).

### *1.3 Focimeter*

Focimeter is an ophthalmic instrument that can verify the power of a CL using a special lens support. It is also called lensmeter. There are two different methods that can be applied: a) the in-air method and b) the wet cell-method. The in-air method was commonly used despite the disadvantage, of the dehydration of the lens typically occurring within a few seconds. Thus, dioptric power measurements have to be performed as soon as the lens is removed from the saline. The wet-cell method

provides more reliable readings because the lens remains hydrated in a small plastic chamber filled with saline.

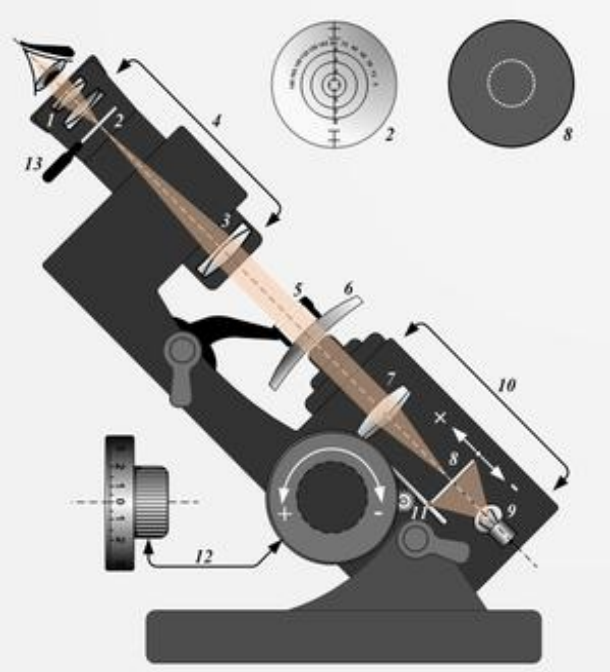

**A simple lensmeter cross sectional view.**

**1** – Adjustable eyepiece
**2** – Reticle
**3** – Objective lens
**4** – Keplerian telescope
**5** – Lens holder
**6** – Unknown lens
**7** – Standard lens
**8** – Illuminated target
**9** – Light source
**10** – Collimator
**11** – Angle adjustment lever
**12** – Power drum (+20 and -20 Diopters)
**13** – Prism scale knob

***Fig. 1.6:*** *Focimeter (Tamasflex)*

Moreover, it offers good optical quality of the image and reproducibility. Nevertheless, suffers from errors regarding the dioptric power determination mainly due to the oversimplification of the optics involved(Yumori,1981). Also, saline can mask surface distortions(Hampson,1973).

## *1.4 Moiré deflectometry*

Moiré deflectometry is also a non-destructive interferometry technique with low cost used since 1976 (Gilman) for lens power estimation and corneal topography. According to this method, 'the object to be tested is mounted in the course of a collimated beam followed by a pair of transmission gratings placed at a distance from each other. The resulting fringe pattern, i.e., the moiré deflectogram, is a map of ray deflections corresponding to the optical properties of the inspected object.' wikipedia

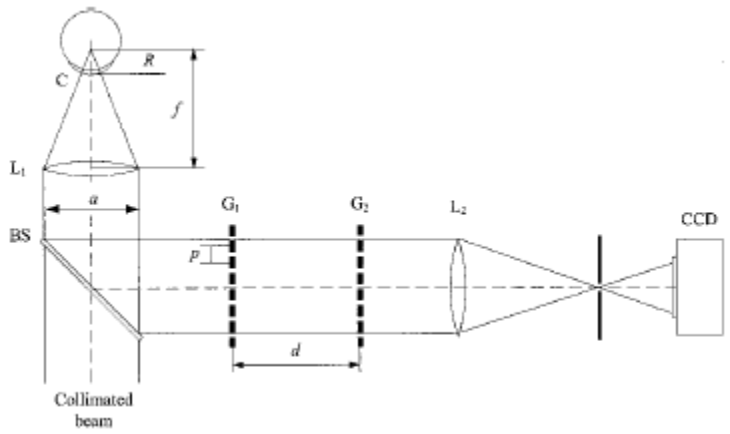


***Fig. 1.7:*** *Schematic system arrangement of a typical Moire deflectometer used to measure corneal surface (Mejia-Barbosa Y. et al 2001)*

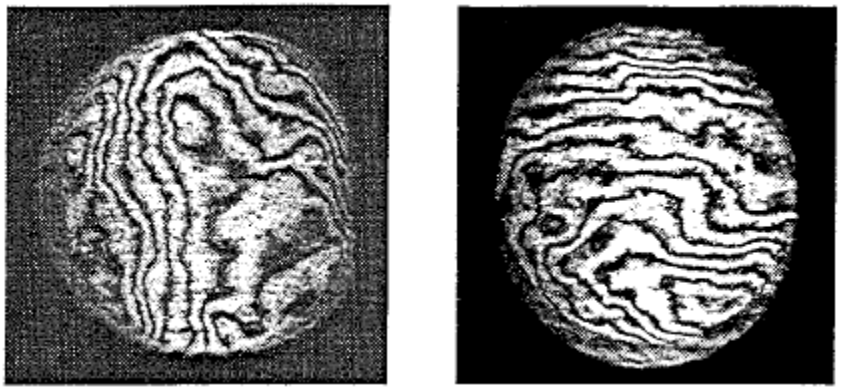

***Fig. 1.8 :*** *The x and y deflectograms from a dry, hard contact lens (Rodenstock, Germany) with a front side radius R=8.86mm (Rottenkolber, M. et al. 1996)*

## *1.5 Optimec JCF*

Optimec JCF is a projection based instrument suitable for Back Optic Zone Radius (BOZR), diameter and central thickness (CT) determination. JCF has two different temperature controlled wet-cells; the first one for measuring diameter with the lens placed onto a gratitule (±0.025 mm resolution) and the second for measuring the BOZR with a cylinder and a probe (±0.02mm resolution). Central thickness is estimated by a projected image (x20) of the Cls (±0.05mm resolution). The technique is fast, the estimated time for a trained operator is 45 to 50 seconds, but there are two basic drawbacks. The first one is that the standard deviation in the BOZR and central thickness measurements is rather large as a result of subjective operation of

the instrument. Secondly, the repeatability can be impaired by the difference of the Cls sag during the sequential measurements in the two wet-cells.

Optimec JCF results were compared with OCT for the same soft lenses. Central thickness and diameter found similar, however OCT showed better repeatability for BOZR calculation (Benjamin J.Coldrick, 2015)

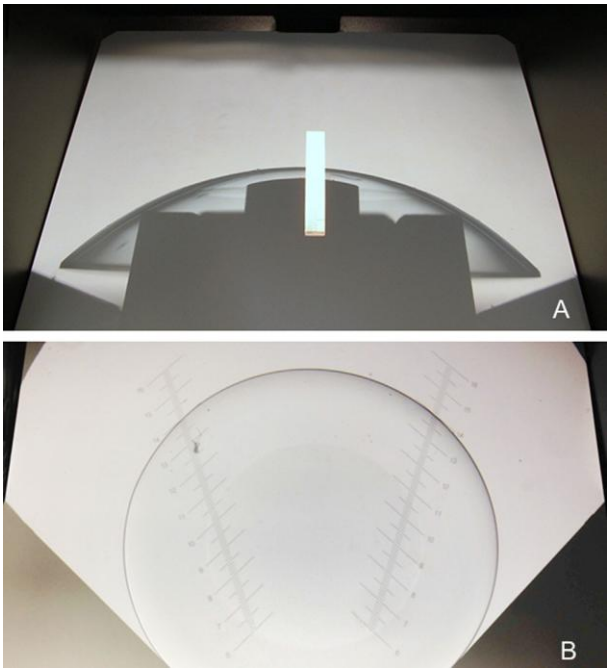


***Fig 1.9: A****: illustration of the BOZR ant centre thickness measurement utilising a cylinder and a pillar for the measurement of the BOZR via sagittal height , in addition to a visual scale for centre thickness inspection* ***B****: Illustration of the diameter measurement cell utilizing a graticule with a left and right scale for visual inspection*

## *1.6 Shifting Schlieren method*

"The schlieren technique (ST) is popular for depicting deviations in light beams induced by density or temperature gradients in a fluid, surface shape, deformation etc" ("Phase-shifting schlieren: high-resolution quantitative schieren that uses the phase-shifting techique principle", Luc Joannes et al). ST provides high and variable sensitivity with low cost.

Nimo TR1504 is a mapping instrument that combines ST with a phase-shifting method, this phase shifting schlieren method is generally used in interferometry (Joannes L. et al. 2010 ; Dominguez-Vicent A. et al, 2015 ; Kim E. et al. 2016)

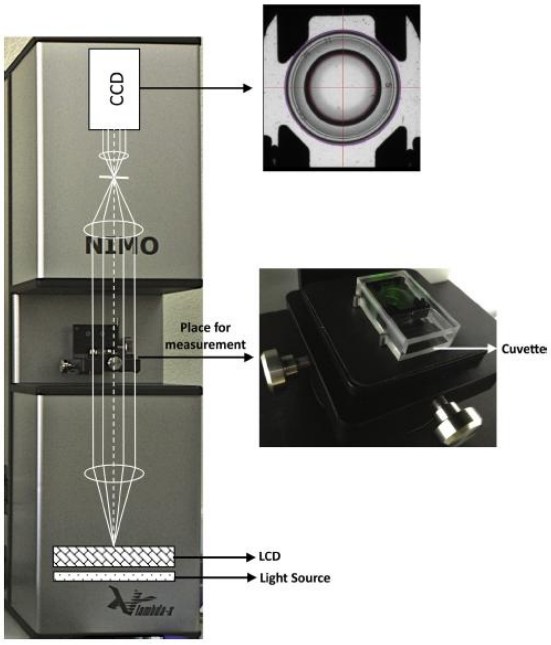


***Fig. 1.10:*** *Schematic layout of NIMO TR1504 (*Dominguez-Vicent A. et al, 2015)

A schematic layout of the NIMO instrument is shown in Figure 1.8. NIMO consists of a light source, emitting green light at 545nm and above it there is a liquid crystal display LCD for the modulation of the light intensity before reaching the CCD camera. The lens placed in the cuvette causes the emitted light to deviate and form the Schlieren fringes. The number of schlieren fringes is proportional to the deviation of the light because of the power of the lens, as shown in Figure 1.9. The estimated wavefront for the recorded power map is fitted to a Zernike polynomial combination. The resolution of the instrument depends on the number of pixels in the camera.

The reproducibility of this method has been tested on spherical, toric and multifocal contact lenses, providing a respective standard deviation on the dioptric power determination in the order of 0.05 D. Despite the success of the repeatability of the method, it can only evaluate dioptric power and not the geometrical parameters of the Cl.

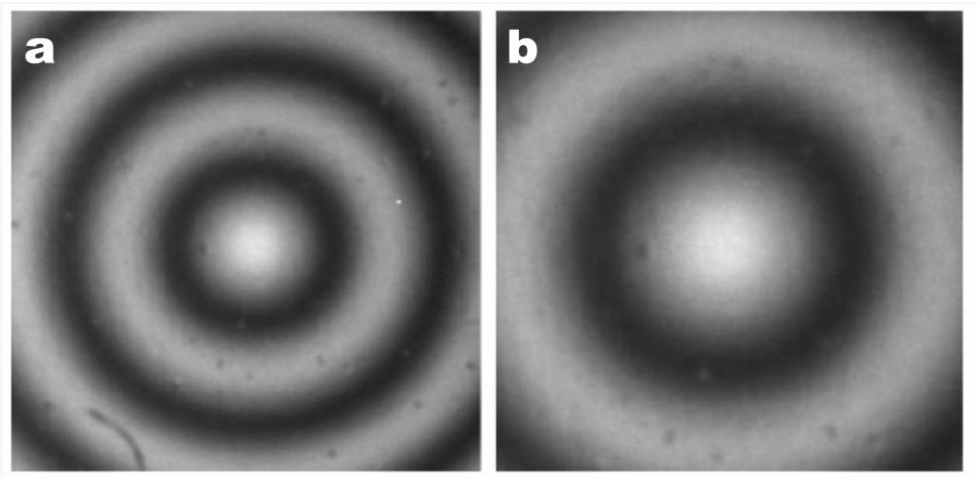


***Fig. 1.11:*** *The difference in schlieren fringes obtained with two different lens, the higher powered lens on the left has more schlieren fringes than the lower powered lens on the right. The resolution is 36 microns (*Joannes L. et al. 2010*).*

## *1.7 Atomic Force Microscopy*

Atomic force microscopy (AFM) represents an alternative approach for the imaging of Cls surface , evaluating roughness, structure and possible defects (figure 1. 10). AFM's resolution is of the order of nanometers and its operation is based on the precise scanning of a sharp tip closely over the CLs surface Baguet J. et al 1993 ; Bhatia S. et al 1997) Although AFM is a powerful technique for high resolution imaging, it is suitable only for surface inspection.

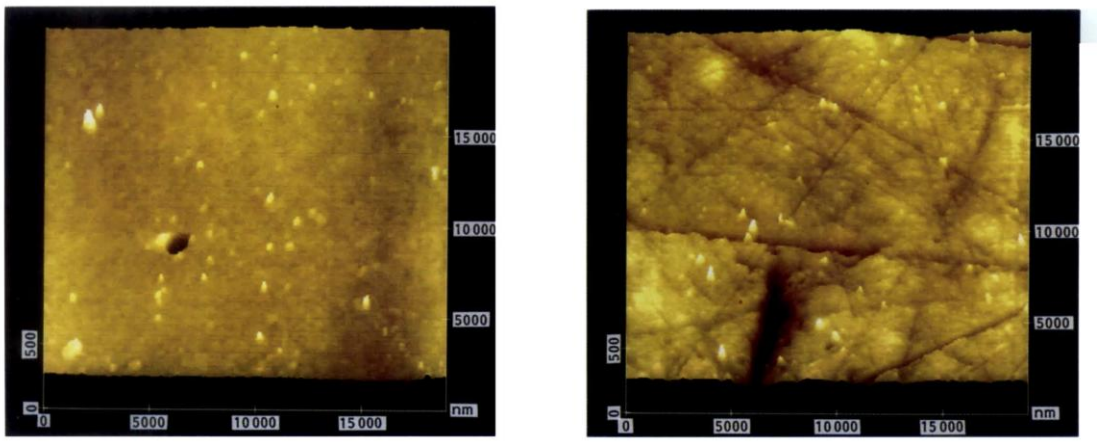


***Fig. 1.12:*** *Atomic force microscopy three-dimensional images of defects on soft contact lens (SCL) surfaces. a, Hole on a 78% water content (WC), molden, poly(methyl methacrylate)-N-vinylpyrrolidone (PMMAINVP) SCL surface. b, Scratch on a 72O/6W C, molden, PMMAINVP SCL surface (*Baguet J. et al 1993)

## *1.8 Scanning electron microscope with energy dispersive X-ray analysis (SEM-EDX)*

A scanning electron microscope (SEM) produces images of a sample by scanning it with a focused beam of electrons. The interaction of electrons and atoms in the sample, produces signals that contain information about the sample's surface topography and composition. SEM is combined with dispersive X-ray analysis, a technique capable to identify the elemental composition of materials. In the field of Cls SEM-EDX can investigate the surfaces and principal elements of the colorants of cosmetically tinted Cls. Cosmetically colored lenses have a dot matrix design that has been depicted by this method and also the colorants depth was determined. Additionally, it was observed that there is a possibility heavily applied colorants alter lens rigidity and may cause friction on the cornea. For the measurements ,Cls were flatten, cut into quarters and desiccated (Hotta F. et al, 2015)

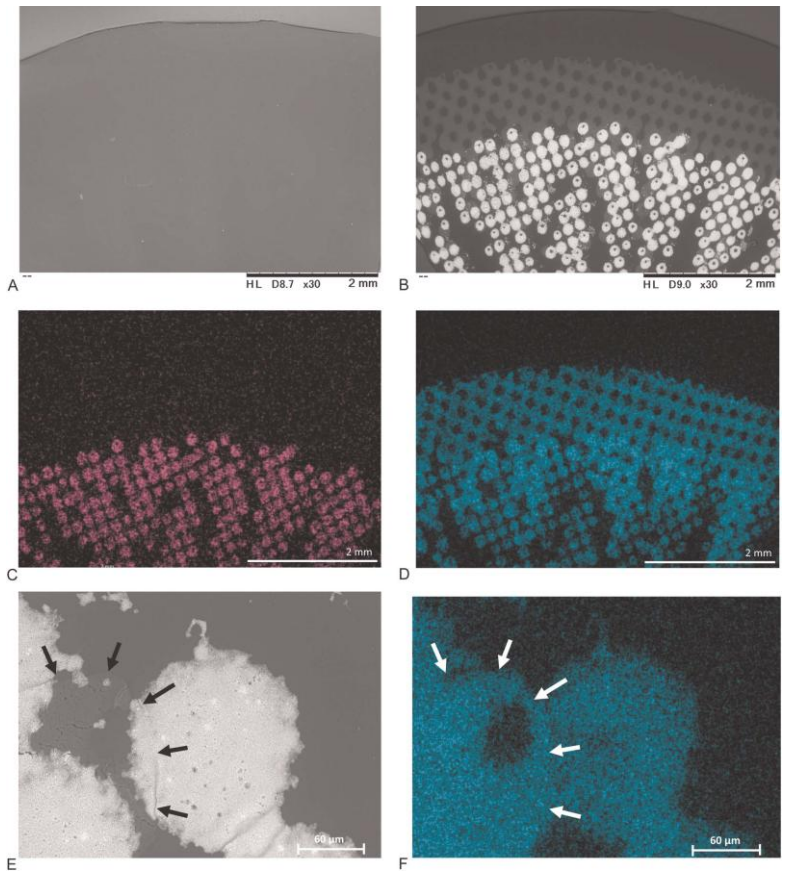


***Fig 1.13:*** *Scanning electron microscopy views and mapping analysis of EVER XOLOR1-DAY NATURAL. (A) The surface of the anterior side is smooth. (B) Colorants are deposited on the posterior side. (C) Purple shows the distribution of titanium. (D) Light blue shows distribution of chlorine (E) Black show exuded chlorine in high magnification. (F) White show exuded chlorine.*

## *References*


Achatz, M., Killpartrick, M.R.Thickness of contact lenses; Computer aided design and interferometric controls (1983) Journal of the British Contact Lens Association, 6 (2), pp. 74,76-78,80-82

Baguet, J., Sommer, F., Duc, T.M. Imaging surfaces of hydrophilic contact lenses with the atomic force microscope (1993) Biomaterials, 14 (4), pp. 279-284.

Bhatia, S., Goldberg, E.P., Enns, J.B. Examination of contact lens surfaces by Atomic Force Microscope (AFM) (1997) CLAO Journal, 23 (4), pp. 264-269.

Cheng, Y.-C., Chen, J.-H., Chang, R.-J., Wang, C.-Y., Hsu, W.-Y., Wang, P.-J. Design and verifications of an eye model fitted with contact lenses for wavefront measurement systems (2015) Proceedings of SPIE - The International Society for Optical Engineering, 9579, art. no. 95790S

Coldrick, B.J., Richards, C., Sugden, K., Wolffsohn, J.S., Drew, T.E. Developments in contact lens measurement: A comparative study of industry standard geometric inspection and optical coherence tomography (2016) Contact Lens and Anterior Eye

Davidson, B.R., Barton, J.K. Application of optical coherence tomography to automated contact lens metrology (2010) Journal of Biomedical Optics, 15 (1), art. no. 016009, .

Domínguez-Vicent, A., Marín-Franch, I., Esteve-Taboada, J.J., Madrid-Costa, D., Montés-Micó, R. Repeatability of in vitro power profile measurements for multifocal contact lenses (2015) Contact Lens and Anterior Eye, 38 (3), pp. 168-172.

El-Nashar, N.F., Larke, J.R., Brookes, C.J. The measurement of the Bausch & Lomb Soflens contact lens by interferometry (1979) American Journal of Optometry and Physiological Optics, 56 (1), pp. 10-15

Hotta, F., Eguchi, H., Imai, S., Miyamoto, T., Mitamura-Aizawa, S., Mitamura, Y. Scanning electron microscopy findings with energy-dispersive X-ray investigations of cosmetically tinted contact lenses (2015) Eye and Contact Lens, 41 (5), pp. 291-296.

Joannes, L., Hough, T., Hutsebaut, X., Dubois, X., Ligot, R., Saoul, B., Van Donink, P., De Coninck, K. The reproducibility of a new power mapping instrument based on the phase shifting schlieren method for the measurement of spherical and toric contact lenses (2010) Contact Lens and Anterior Eye, 33 (1), pp. 3-8.

Kałuzny, B.J., Kaluzny, J.J., Szkulmowska, A., Gorczyńska, I., Szkulmowski, M., Bajraszewski, T., Targowski, P., Kowalczyk, A. Spectral optical coherence tomography: A new imaging technique in contact lens practice (2006) Ophthalmic and Physiological Optics, 26 (2), pp. 127-132

Kaluzny, B.J., Fojt, W., Szkulmowska, A., Bajraszewski, T., Wojtkowski, M., Kowalczyk, A. Spectral optical coherence tomography in video-rate and 3D imaging of contact lens wear (2007) Optometry and Vision Science, 84 (12), pp. E1104-E1109.

Karnowski, K., Grulkowski, I., Mohan, N., Cox, I., Wojtkowski, M. Quantitative optical inspection of contact lenses immersed in wet cell using swept source OCT (2014) Optics Letters, 39 (16), pp. 4727-4730.

Kim, E., Bakaraju, R.C., Ehrmann, K. Reliability of power profiles measured on NIMO TR1504 (Lambda-X) and effects of lens decentration for single vision, bifocal and multifocal contact lenses (2016) Journal of Optometry, 9 (2), pp. 126-136.

Marcus, M.A., Compertore, D., Gibson, D.S., Herbrand, M.E., Ignatovich, F.V. Multimodal characterization of contact lenses (2015) Proceedings of SPIE - The International Society for Optical Engineering, 9633, art. no. 96331W,.

Mejía-Barbosa, Y., Malacara-Hernández, D. A review of methods for measuring corneal topography (2001) Optometry and Vision Science, 78 (4), pp. 240-253.

Plakitsi, A., Charman, W.N. An interferometric null method for measuring the power distribution across varifocal contact lenses (1993) International Contact Lens Clinic, 20 (1-2), pp. 32-38

Rodrigues, P., Lopes-Ferreira, D., Catarino, A., Cervino, A., Queirós, A., González-Méijome, J.M. Reliability of manual segmentation of cornea, contact lens and tear film using a high-resolution OCT (2015) Journal of Modern Optics, 62 (21), pp. 1808-1815.

Rottenkolber, M., Podbielska, H. Measuring ophthalmologic surfaces by means of moiré deflectometry (1996) Optical Engineering, 35 (4), pp. 1124-1133.

Shen, M., Cui, L., Riley, C., Wang, M.R., Wang, J.H. Characterization of soft contact lens edge fitting using ultra-high resolution and ultra-long scan depth optical coherence tomography (2011) Investigative Ophthalmology and Visual Science, 52 (7), pp. 4091-4097.

Tao, A., Shao, Y., Jiang, H., Ye, Y., Lu, F., Shen, M., Zhu, D., Wang, J. Entire thickness profiles of the epithelium and contact lens in vivo imaged with high-speed and high-resolution optical coherence tomography (2013) Eye and Contact Lens, 39 (5), pp. 329-334.

Yumori, R.W., Mandell, R.B. Optical power calculation for contact lens wet cells (1981) American Journal of Optometry and Physiological Optics, 58 (8), pp. 637-639.

# *Chapter 2: Photoacoustic Microscopy*

## *2.1 Introduction*

Photoacoustic microscopy (PAM) is a novel imaging technique which uses the photoacoustic effect to provide contrast of intensely light absorbing structures. According to this process, acoustic waves are emitted in all spatial directions, following the thermoelastic expansion of a material sample through its time-variable heating, usually by pulsed or intensity modulated CW laser sources. The typical tissue components inducing strong photoacoustic excitation are hemoglobin and melanin. Despite the fact that PAM has been applied exclusively to biological specimens so far, it has the potential to image every structure or material that presents a relatively high degree of absorption for the employed optical wavelength. Therefore, this feature permits the extraction of precise structural, morphological and functional information of non-biological objects in three dimensions. In the next chapters of this thesis, we will demonstrate, for the first time to our knowledge, the diagnostic potential of PAM in the field of contact lenses.

## *2.2 The photoacoustic effect*

Photoacoustic effect was introduced by Alexander Graham Bell in 1880 when he invented the photophone, the first wireless telecommunication device that used a beam of light to transmit speech. Nevertheless, the phenomenon wasn't further exploited till the development of modern technical equipment such as ultrasonic transducers, computers etc.

The main mechanism generating the phenomenon is photothermal. The absorbed radiation in the sample is partially converted into heat, resulting in a local temperature rise which is proportional to the absorption magnitude. Subsequently, this local heating induces an initial pressure due to the sudden thermoelastic expansion of the medium, propagating through a surrounding medium in the form of acoustic waves. In this manner, the detection of the amplitude of the emitted photoacoustic waves provides information about the specimen's absorption properties.

## *2.3 Derivation of the general photoacoustic equation*

In order to derive the general photoacoustic equation, we begin with two basic equations. The first one is the thermal expansion equation

$$\nabla \cdot \vec{\xi}(\vec{r},t) = -\kappa p(\vec{r},t) + \beta T(\vec{r},t) \quad (2.1)$$

where vector $\vec{\xi}$ denotes the medium displacement from the equilibrium state, κis the isothermal compressibility (typical value for soft tissue ~$5\text{x}10^{-10}$ $Pa^{-1}$), βis the thermal coefficient of volume expansion (typical value for muscle ~$4\text{x}10^{-4}K^{-1}$) and p, T are the pressure and temperature functions respectively. Thermodynamically, κis defined as

$$\kappa = -\frac{1}{V}\left(\frac{\partial V}{\partial P}\right)_T \quad (2.2)$$

and corresponds to the fractional change of volume while changing the pressure at a constant temperature

and β as

$$\beta = \frac{1}{V}\left(\frac{\partial V}{\partial T}\right)_P \quad (2.3)$$

expressing the fractional change of volume while changing temperature at a constant pressure.

Equation (2.1) describes that the fractional volume expansion of the medium (left part) is equal to the sum of two factors (right part): the first one is related to the exerted pressure, whereas the second one is a function of the object's temperature. Positive pressures tend to "shrink" the object –this explains the minus sign of the first term. On the other hand, the second factor expresses a linear relation of the volume expansion with the temperature-the more the object is heated the more it will expand.

The second basic equation is actually another version of the Newton's second law called inviscid force equation and has the form

$$\rho \frac{\partial^2}{\partial t^2}\vec{\xi}(\vec{r},t) = -\nabla p(\vec{r},t) \quad (2.4)$$

The left term here represents the mass density times the acceleration and the right one is the force applied per unit volume. In order to make clearer why the gradient of the pressure is related to the force, let us take the following example: Consider a cubic parcel of a medium with mass given by the following equation

$$m = \rho \cdot dA \cdot dz \quad (2.5)$$

where dA is the respective surface area and dz its height. By employing Newton's second law, we can examine a pressure difference dP (assumed to be only in z direction) to find the resulting force as

$$F = m \cdot a = \rho \cdot dA \cdot dz \cdot a = -dp \cdot dA \quad (2.6)$$

The latter relation can be rewritten as

$$\rho\alpha = -\frac{dp}{dz} \quad (2.7)$$

or in a more general form as

$$\rho\vec{\alpha} = -\nabla\vec{p} \quad (2.8)$$

which comprises a compact form for the initial equation (2.4) (Q.E.D.).

Taking the divergence of (2.4), we obtain

$$\rho\frac{\partial^2}{\partial t^2}[\nabla \cdot \vec{\xi}(\vec{r},t)] = -\nabla^2 p(\vec{r},t) \quad (2.9)$$

Substituting $\nabla \cdot \vec{\xi}(\vec{r},t)$ from (2.1) into (2.9), we get

$$\rho\frac{\partial^2}{\partial t^2}[-\kappa p(\vec{r},t) + \beta T(\vec{r},t)] = -\nabla^2 p(\vec{r},t) \quad (2.10)$$

or by re-arranging the terms

$$\left(\nabla^2 - \rho\kappa\frac{\partial^2}{\partial t^2}\right)p(\vec{r},t) = -\beta\rho\frac{\partial^2 \mathrm{T}(\vec{r},t)}{\partial t^2} \quad (2.11)$$

In general, the speed of sound is given by the Newton-Laplace equation

$$u_s = \sqrt{\frac{K}{\rho}} \quad (2.12)$$

where K is the bulk modulus measuring the resistance of the medium to uniform compression, which is equal to the inverse compressibility κ(isothermal). Therefore, the speed of sound can be expressed as

$$u_s = \sqrt{\frac{1}{\rho\kappa}} \quad (2.13)$$

By combining (2.11) and (2.13), we get the general photoacoustic equation with a final form

$$\left(\nabla^2 - \frac{1}{u_s^2}\frac{\partial^2}{\partial t^2}\right)p(\vec{r},t) = -\frac{\beta}{\kappa u_s^2}\frac{\partial^2 T(\vec{r},t)}{\partial t^2} \quad (2.14)$$

The left-hand side of the equation describes the pressure wave propagation whereas the right-hand side represents the source term. Therefore, time-invariant heating does not produce a pressure wave; only time-variant heating does.

**Photoacoustic equation under thermal confinement**

Under thermal confinement conditions (i.e. heat conduction is negligible during the laser pulse), we can derive from the fundamental equation

$$Q = mC_V \mathrm{T} \quad (2.15)$$

whereQ is the thermal energy, m is the mass, $C_V$ is the specific heat capacity under constant volume and T is the absolute temperature that

$$\frac{dQ}{dt} = mC_V\frac{dT}{dt} = \rho V C_V\frac{dT}{dt} \quad (2.16)$$

If we define a heating function H as the thermal energy converted per unit volume per unit time (units: $J/m^3/s$), then we have from (2.16) that

$$H = \rho C_V\frac{dT}{dt} \quad (2.17)$$

Laws of thermodynamics also indicate that

$$\frac{C_P}{C_V} = \frac{\kappa}{\beta_S} \quad (2.18)$$

where$C_P$and $C_V$ are the specific heat capacities under constant pressure and volume, whereas$\beta_S$ stands for the isoentropic compressibility, defined as

$$\beta_S = -\frac{1}{V}\left(\frac{\partial V}{\partial P}\right)_S \quad (2.19)$$

expressingthe fractional change of volume while changing the pressure at a constant entropy.

On the other hand, the equation of state denotes that

$$u_s^2 = \left(\frac{\partial P}{\partial \rho}\right)_S \quad (2.20)$$

By combining (2.19) and (2.20) we get

$$\beta_S = -\frac{1}{V}\left(\frac{\partial V}{\partial P}\right)_S \frac{\partial \rho}{\partial \rho} = -\frac{1}{V}\left(\frac{\partial \rho}{\partial P}\right)_S \frac{\partial V}{\partial \rho} = -\frac{1}{Vu_s^2}\frac{\partial V}{\partial \rho}$$
$$= -\frac{1}{Vu_s^2}\frac{\partial(m/\rho)}{\partial \rho} = \frac{1}{\rho u_s^2} \quad (2.21)$$

Subsequently, (2.18) and (2.21) will finally result in

$$\kappa = \frac{C_P}{\rho u_s^2 C_V} \quad (2.22)$$

The right part (source term) of (2.14) will then become through (2.17) and (2.22)

$$-\frac{\beta}{\kappa u_s^2}\frac{\partial^2 T(\vec{r},t)}{\partial t^2} = -\frac{\beta}{C_P}\frac{\partial H(\vec{r},t)}{\partial t} \quad (2.23)$$

so that

$$\left(\nabla^2 - \frac{1}{u_s^2}\frac{\partial^2}{\partial t^2}\right)p(\vec{r},t) = -\frac{\beta}{C_P}\frac{\partial H(\vec{r},t)}{\partial t} \quad (2.24)$$

Additionally, $H(\vec{r},t)$ can be further decomposed as the product of the respective spatial and temporal parts in the following form

$$H(\vec{r},t) = H_S(\vec{r})H_T(t) \quad (2.25)$$

whereas $H_S(\vec{r})$ represents the local deposited energy density in J/m$^3$ and $H_T(t)$ is the temporal excitation profile (e.g. a Gaussian pulse).

Using (2.25), equation (2.24) can then be re-arranged as following

$$\left(\nabla^2 - \frac{1}{u_s^2}\frac{\partial^2}{\partial t^2}\right)p(\vec{r},t) = -\frac{\beta H_S(\vec{r})}{C_P}\frac{\partial H_T(t)}{\partial t} \quad (2.26)$$

comprising the photoacoustic equation under thermal confinement conditions.

In case that $H_T(t) = \delta(t)$ (i.e. impulse temporal excitation), we finally have

$$\left(\nabla^2 - \frac{1}{u_s^2}\frac{\partial^2}{\partial t^2}\right)p(\vec{r},t) = -\frac{\beta H_S(\vec{r})}{C_P}\frac{\partial \delta(t)}{\partial t} \quad (2.27)$$

(Wang &Wu,2007)

## *2.4 Photoacoustic imaging*

Photoacoustic imaging systems can be generally divided into two main categories: the first one includes the tomographic systems which typically employ uniform illumination and detection using unfocused ultrasound detectors. Tomographic systems require as we will see a bit later, a reconstruction algorithm in order to get a final image of the examined specimen. The most popular algorithm for this purpose is called back projection reconstruction and it is actually a slightly modified version of the methodology that is followed in the case of X-Ray Computed Tomography imaging. Concerning their performance, the tomographic approaches have the potential to provide high imaging depths, up to 5 cm for highly scattering tissue samples at spatial resolutions in the order of a few hundreds of μm. A tomographic scan can be achieved using several geometrical configurations, with most common the spherical, cylindrical and planar scanning schemes.

On the other hand, the second category includes the photoacoustic microscopy systems, which in contrast to the tomographic ones, they use either weakly or tightly focused illumination, whereas the respective detection is achieved through spherically focused detectors. Another important difference when compared to the tomographic systems is that microscopy approaches do not require a reconstruction algorithm; what you detect is what you see on the image you get. Photoacoustic microscopy systems generally provide a shallower imaging depth, typically up to 3 mm, however at much higher spatial resolutions than tomographic imaging. More specifically, by employing the so called optical resolution photoacoustic microscopy approaches, we get diffraction limited lateral resolutions in the order of 1 μm at a limited imaging depth which does not exceed 1 mm in tissue. Alternatively, through an acoustic resolution photoacoustic microscopy approach, someone would get a relatively lower spatial resolution in the order of 30 μm, however at a significantly higher imaging depth than optical resolution microscopy. In general, there is always this tradeoff between spatial resolution and imaging depth; therefore someone has to choose the most suitable imaging technique according to the features of the biological specimen under investigation.

## *2.5 Imaging Depth and Resolution of PAM*

The main advantage of PAM over pure optical microscopy techniques, such as confocal or two photon microscopes, is the extended imaging depth in highly scattering tissues. Although optical microscopy is a powerful biomedical imaging modality, with excellent contrast and spatial resolution capabilities, it provides a rather limited imaging depth (< 500 μm) due to the intense photon scattering in tissues, with a respective coefficient $\mu_\alpha$ which is more than three orders magnitude higher than ultrasonic scattering (Wang & Wu ,2007). PAM's maximum imaging depth ranges from 100 μm to 3 mm and (Wang L.V. et al.,2012;Wang L.V. 2009) spatial resolution is ranging from less than 1 μm to a few hundreds of μm, depending on the maximum imaging depth.

Unlike to other optical techniques, PAM does not need depth scanning. The 3D information is a result of the different time of flight for the photoacoustic signal to reach the detector.

PAM images are acquired by raster scanning of the specimen with a confocally aligned optical illumination and acoustic detection (figure 2.1).

PAM is classified into two main categories: Optical Resolution PAM (OR-PAM), where the optical focusing is much tighter than acoustic focusing (Maslov K. et al., 2008) and Acoustic Resolution (AR-PAM) where the respective acoustic focusing is tighter. OR-PAM can reach imaging depth ~1mm, whereas AR-PAM at ~3mm but with lower lateral resolution.

PAM's detection sensitivity is affected by the incident laser fluence, imaging depth, wavelength, absorption cross section of the target and the efficiency of the transducer (Ku G. et al,2005).

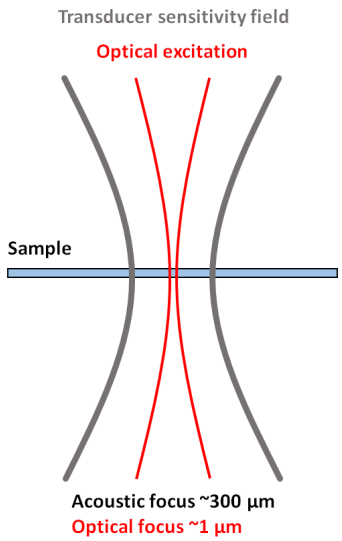


***Fig. 2.1**:Confocal configuration of excitation and detection*

PAM can be effectively combined with pure optical modalities such as fluorescence microscopy, in order to provide label-free complementary contrast

## *2.6 Applications*

PAM is a biomedical imaging modality with numerous of applications in biomedical research. The typical tissue components inducing strong photoacoustic (PA) excitation are hemoglobin and melanin but there are many other endogenous molecules, shown in figure 2.2. Besides these molecules, there are also exogenous delivered contrast agents for optical absorption such as doxorubicin with an absorption peak near 470nm.

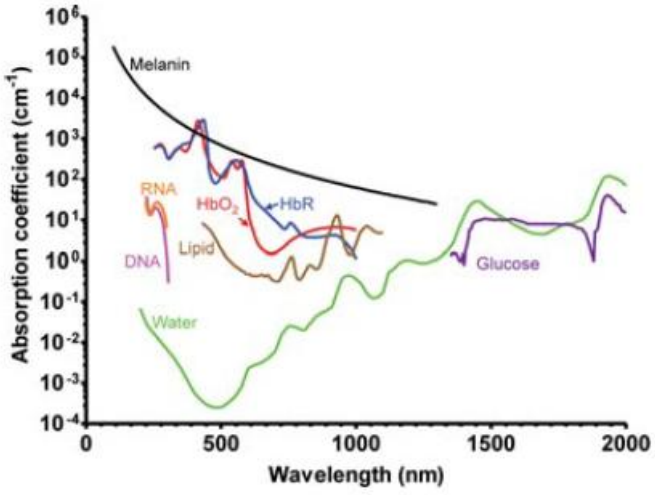


**Fig. 2.2** Absorption spectra of major endogenous contrast agents in biological tissue. Oxyhemoglobin, red line (150 g/L in blood); Deoxy-hemoglobin, blue line (150 g/L in blood); Lipid, brown line (20% by volume in tissue); Water, green line (80% by volume in tissue); DNA, magenta line (1 g/L in cell nuclei); RNA, orange line (1 g/L in cell nuclei); Melanin, black line (14.3 g/L in medium human skin); Glucose, purple line (720 mg/L in blood) (Yao J et al, 2013).

In the ultraviolet and visible regions the main absorbers are DNA/RNA , cytochrome c, myoglobin, hemoglobin and melanin. Figure 3.3 shows multi contrast PAM images

in the region 180 to 700nm; a to c are label free images, while d and f have contrast agents inserted. Typical examples of multi-contrast PAM applications are depicted in figure 3. Image (a) is a cell nuclei at UV wavelength, signal comes from RNA and DNA. Image (b) depicts red blood cells, (c) retinal vessels and (d) the microvasculature in a mouse ear; in all these cases signal comes from hemoglobin. Image (e) shows a melanoma labeled with targeted gold nanocages and (f) a mouse mammary gland tumor with a near-infrared fluorescent protein.

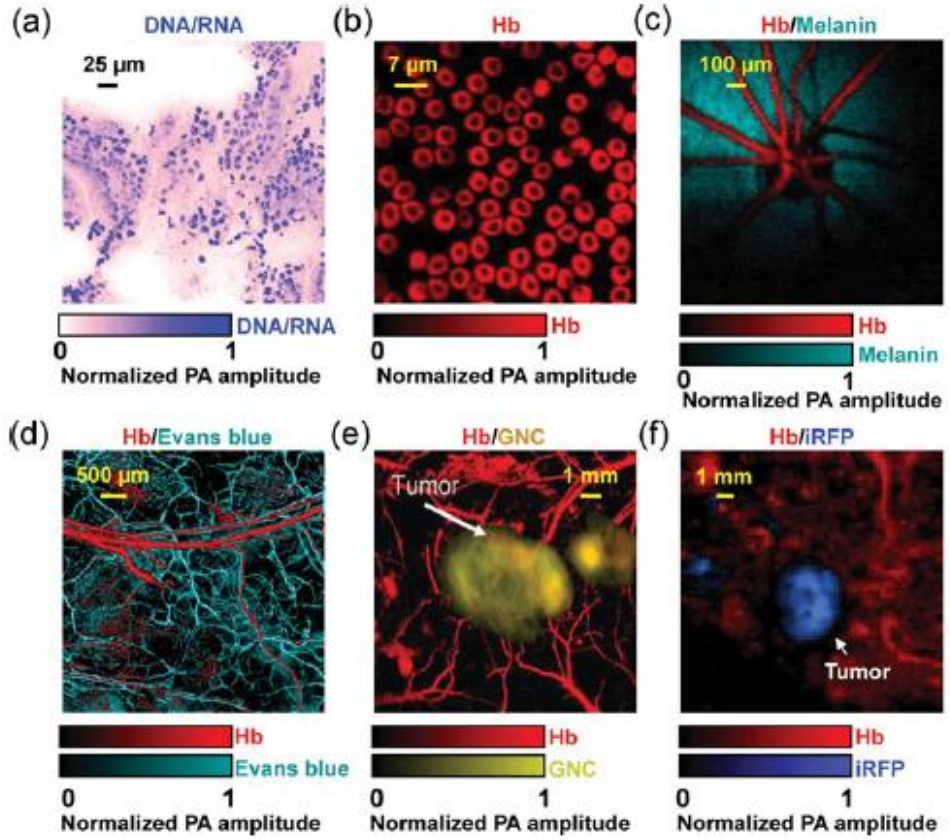


***Fig. 2.3:*** *Representative multi-contrast PAM images. (a) UV-PAM of cell nuclei (shown in blue) in a 6-μm-thick slice from mouse small intestine. No histology staining was needed here. The signals of cell nuclei come from DNA and RNA (Yao D.-K. et al 2010). (b) SW-PAM of red blood cells (RBC). The signals of RBCs come from hemoglobin (Hb). ( Zhang C. et al,2010). (c) Photoacoustic ophthalmoscopy of retinal vessels (shown in red) and the retinal pigment epithelium layer (RPE, shown in green) in a living rat. The signals of the RPE layer come from melanin (Jiao S. et al., 2010). (d) OR-PAM of the microvasculature in a mouse ear, where the capillaries (shown in green) were enhanced by Evans blue dye. Reprinted with permission from (Yao J.J et al., 2009). (e) AR-PAM of a subcutaneously inoculated B16 melanoma labeled with targeted gold nanocages (GNC, shown in yellow) and the surrounding vessels (shown in red) in a living mouse (Erpelding T.N. et al., 2010). (f) PAMac of a mouse mammary gland tumor which expressed a near-infrared fluorescent protein iRFP (shown in blue) (Filonov G.S. et al., 2012).*

## *2.7 Hybrid photoacoustic and optical imaging of pigments in vegetative tissues*

The first application of the photoacoustic system developed at the In Vivo Imaging Lab (IVIL) of FORTH was the study of pigments in vegetative tissues. The main pigments are anthocyanins , betalains , carotenoids and chlorophylls and they have been a subject of intense research the past decades because they are responsible for plants' physiology and function. The available wavelength for PAM, 532nm was able to depict anthocyanins and betalains, molecules that give red color to the leaves. Moreover, PAM was combined with fluorescence microscopy in order to have a complementary Chlorophylls autofluorescence image.

Pigments in vegetative tissues have been a subject of intense research during the previous decades, since they play an active role in several molecular mechanisms regarding plants' physiology and function. Towards this direction, the imaging modality that has been extensively employed and represents the state of the art for mapping pigments' distribution is confocalmicroscopy. Despite the advantage of a high spatial resolution however, confocal microscopy provides a rather limited imaging depth and requires necessarily strong fluorescence properties from the specimen under observation. To overcome such limitations, we propose a hybrid, photoacoustic and optical imaging methodology for the delineation of various vegetative pigments, such as chlorophylls, anthocyanins and betalains in different plant species. The superior sensitivity and the high contrast complementarity of the hybrid technique, render it a powerful alternative to the conventional fluorescence imaging modalities, significantly expanding the current state of the art.

Figure 2.6 is a bimodal photoacoustic and fluorescence image of a young rose leaf. (A) is a PAM image depicting the anthocyanin accumulation and (B) is a chlorophylls autoflorescence image of the same image. (C) is a combined image of the previous two.

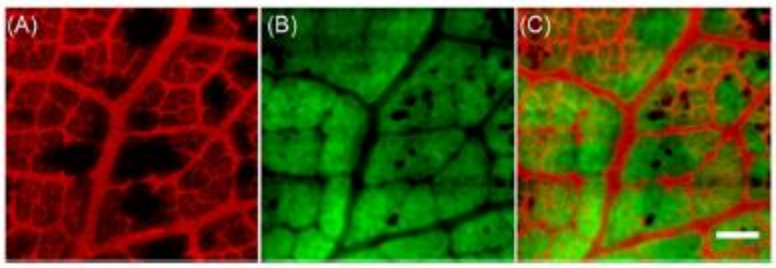

***Fig. 2.6:*** *Bimodal photoacoustic and fluorescence imaging of a young rose leaf. (A) OR-PAM MAP image depicting the anthocyanin accumulation. (B) Chlorophylls autofluorescence image of the same region. (C) Combined image of the two contrast modes. The field of view for this imaging session was 3 mm × 3 mm. Scale bar is equal to 500 µm.*

Figure 2.7 is a tree-dimensional reconstruction of the vessels of a young rose leaf, the signal comes from the anthocyanin pigment distributed in the vessels.

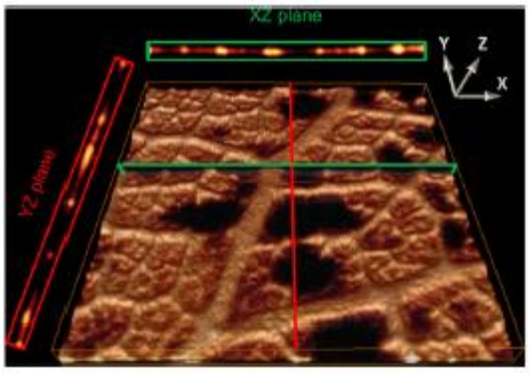


***Fig. 2.7:*** *OR-PAM three-dimensional reconstruction of the anthocyanin pigment distribution, generated from the data recorded for Figure 3. The cross-section images on XZ and YZ planes reveal the axial extents of the vessels at different depths within the resolution of the hybrid system.*

## *References*


Erpelding, T.N., Kim, C., Pramanik, M., Jankovic, L., Maslov, K., Guo, Z., Margenthaler, J.A., Pashley, M.D., Wang, L.V. Sentinel lymph nodes in the rat: Noninvasive photoacoustic and US imaging with a clinical US system (2010) Radiology, 256 (1), pp. 102-110.

Hu, S., Rao, B., Maslov, K., Wang, L.V. Label-free photoacoustic ophthalmic angiography (2010) Optics Letters, 35 (1), pp. 1-3.

Filonov, G.S., Krumholz, A., Xia, J., Yao, J., Wang, L.V., Verkhusha, V.V. Deep-tissue photoacoustic tomography of a genetically encoded near-infrared fluorescent probe (2012) Angewandte Chemie - International Edition, 51 (6), pp. 1448-1451.

Ku, G., Wang, L.V.
Deeply penetrating photoacoustic tomography in biological tissues enhanced with an optical contrast agent (2005) Optics Letters, 30 (5), pp. 507-509.

Maslov, K., Zhang, H.F., Hu, S., Wang, L.V. Optical-resolution photoacoustic microscopy for in vivo imaging of single capillaries (2008) Optics Letters, 33 (9), pp. 929-931.

Maslov, K., Wang, L.V.
Noninvasive mapping of the electrically stimulated mouse brain using photoacoustic microscopy
(2008) Progress in Biomedical Optics and Imaging - Proceedings of SPIE, 6856, art. no. 68561J, . Cited 4 times.
https://www.scopus.com/inward/record.uri?eid=2-s2.0-42149112897&partnerID=40&md5=3db0dc7a745bd2493131128132eb549b

Tserevelakis, G.J., Tsagkaraki, M., Zacharakis, G. Hybrid photoacoustic and optical imaging of pigments in vegetative tissues (2016) Journal of Microscopy, .

Wang, L.V. & Wu, H.-I. (2007) Biomedical Optics: Principles and Imaging, 287pp. Wiley Hoboken, NJ, USA.

Wang, L.V. & Wu, H.-I. (2007) Biomedical Optics: Principles and Imaging, 362pp. Wiley Hoboken, NJ, USA.

Wang, L.V., Hu, S. Photoacoustic tomography: In vivo imaging from organelles to organs (2012) Science, 335 (6075), pp. 1458-1462.

Yao, D.-K., Maslov, K., Shung, K.K., Zhou, Q., Wang, L.V. In vivo label-free photoacoustic microscopy of cell nuclei by excitation of DNA and RNA (2010) Optics Letters, 35 (24), pp. 4139-4141.

Yao, J., Wang, L.V. Photoacoustic microscopy (2013) Laser and Photonics Reviews, 7 (5), pp. 758-778.

Yao, J., Maslov, K., Hu, S., Wang, L.V. Evans blue dye-enhanced capillary-resolution photoacoustic microscopy in vivo (2009) Journal of Biomedical Optics, 14 (5), art. no. 054049

Zhang, C., Maslov, K., Wang, L.V. Subwavelength-resolution label-free photoacoustic microscopy of optical absorption in vivo (2010) Optics Letters, 35 (19), pp. 3195-3197.

# Chapter 3: Materials and Methods

## 3.1 Experimental Setup

The OR-PAM modality of the imaging system (Figure 3.1) employed a variable repetition rate diode pumped ns laser (QIR-1064-200-S, CrystaLaser LC, Reno, Nevada, USA; energy per pulse: 29.4 µJ, pulse width: 10 ns, selected repetition rate: 6.8 kHz, $M^2$ value: ~1.2) emitting infrared irradiation at 1064 nm. The beam was tightly focused by a lens on a Lithium Triborate (LBO) second harmonic generation (SHG) crystal (Castech Inc, Fuzhou, China) to get a visible wavelength at 532 nm. Both fundamental and SHG wavelengths were used for the effective photoacoustic signal excitation due to their intense absorption by the examined specimens.

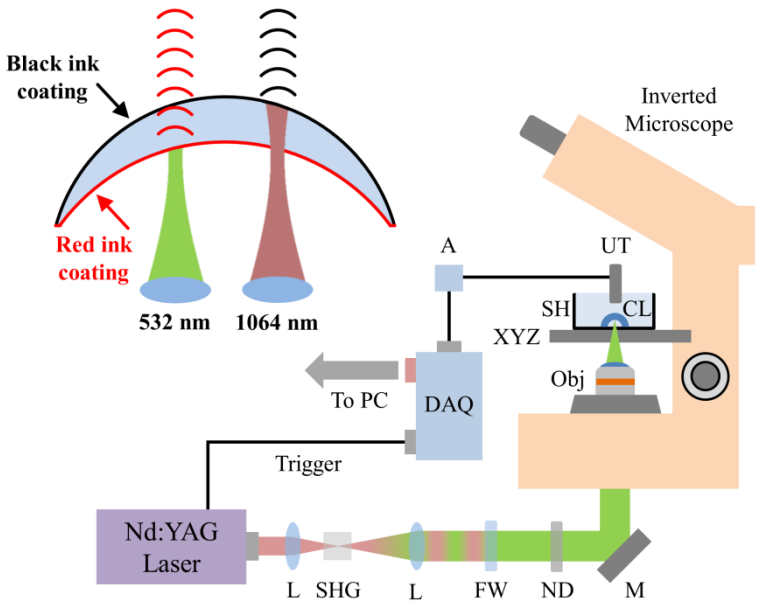


*Fig. 3.1: Scheme of the photoacoustic imaging system for CL measurements, L, lens; M, mirror; SHG, second harmonic generation crystal; FW filter wheel; ND filter, neutral density filter; Obj, objective lens; XYZ, motorized XY and manual Z stages; SH, sample Holder; CL, contact Lens; UT, ultrasound transducer; A, amplifier; DAQ, data acquisition card.*

Following the LBO crystal, a second lens was employed in a telescopic configuration with the focusing one, collimating and expanding the beam by approximately two times. Two interchangeable filters were used for the selection of the desired wavelength according to each CL surface measurement. For 532 nm excitation, a bandpass filter (FF01-531/40-25, Semrock, Rochester, New York, USA), permitting the wavelength transmission from 511 to 551 nm was employed to cut off the residual fundamental light and transmit the SHG line. For infrared excitation, an Nd:YAG laser line filter (FL1064-3, Thorlabs (New Jersey,US) was placed to cut off the visible wavelength. The laser irradiation was further attenuated through a proper combination of neutral density filters in order to control the total energy deposition at the focal plane. Using a couple of high reflection mirrors, the beam was guided into a properly modified inverted optical microscope (Labovert, Leitz, Wetzlar, Germany) serving as a platform for the developed imaging setup. A low numerical aperture (NA) objective lens (Achromat 8X, LOMO, St. Petersburg, Russia; air immersion, NA: 0.2) was employed for the focusing of the beam onto the specimen under investigation. Two custom made tanks were used for the sample placement. The bottom of the first one had an optically transparent round window, while the second one had an optically transparent hemispherical surface manufactured phantom with a radius of curvature of 7.8 mm in order to simulate the radius of a typical corneal surface. The phantom was generated by immersing an industrially made spherical metallic marble (radius: 7.80±0.01 mm) into liquid silicone medium, which was left to solidify for several hours. Following the removal of the marble, the resulting mold was then filled with resin in order to provide the CL-mimicking specimen.

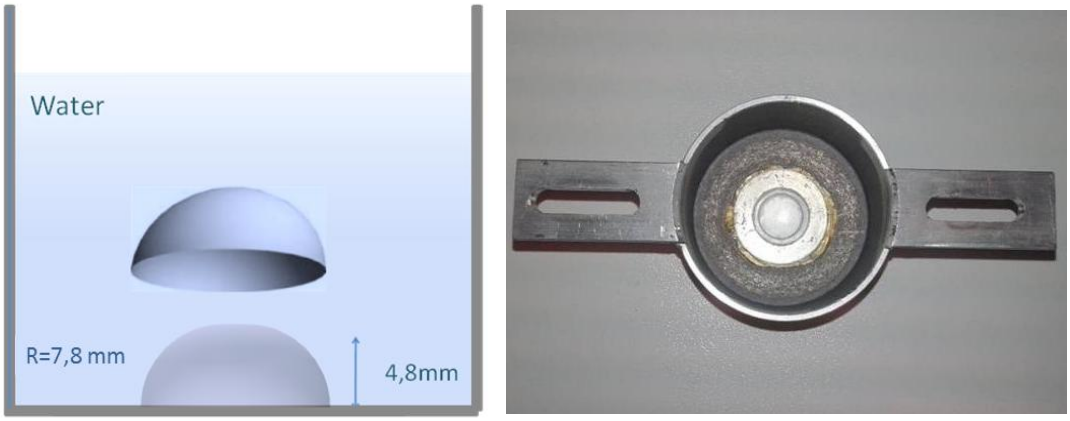


***Fig. 3.2:*** *Tank for CI measurement*

The tank was further attached on a set of sub-μm precision XY motorized stages (8MTF-75LS05, Standa, Vilinius, Lithuania) performing a lateral raster scanning as to the beam focus. The vertical position of the sample was selected manually using the Z-adjustment microscope controls. The tank was filled with distilled water in order to provide an efficient acoustic coupling between the photoacoustic sources and the detection unit. A 20 MHz central frequency, spherically focused ultrasonic transducer (V373-SU, Olympus, Tokyo, Japan; effective bandwidth: approximately 13-33 MHz, focal distance: 32 mm) was immersed into the tank in a confocal and coaxial configuration with respect to the focal volume of the beam, achieving in this manner, the maximum detection sensitivity at the excited region. The detected broadband signals were additionally amplified using a low noise RF amplifier (AU-1291, Miteq, New York, USA; gain 63 dB) and recorded via a high speed oscilloscope (DSO7034A, Agilent Technologies, Santa Clara, California, USA; bandwidth: 350 MHz, sample rate: 2 GSa/s) connected to a computer. Furthermore, the signal was averaged 32 times at each measurement position for SNR improvement. The data acquisition triggering was provided by the control unit of the ns laser in order to synchronize the recording of the time-domain photoacoustic signal with the pulse incidence on the sample. To generate a three-dimensional reconstruction, the envelopes of the signals were calculated using the modulus of the Hilbert transform

(Tserevelakis G. J. et al., 2014).The lateral resolutions of photoacoustic is ultimately limited by laser light diffraction. Due to the fact that the back aperture of the objective lens is underfilled to achieve a higher depth of field, the effective NA is approximately half of the nominal one, resulting in a maximum lateral resolution of ~3 μm. Nevertheless, the measurements presented in this study have a pixel size of 65μm due to undersampling. On the other hand, the maximum axial resolution in the case of OR-PAM, depends solely on the ultrasonic transducer detection bandwidth. Therefore, a good estimation of the axial resolution is given by the half of the minimum ultrasound wavelength that can be effectively detected, by taking into account that the average speed of sound in typical soft tissue samples is in the order of 1500 m/s. Under such conditions, the axial detail resolving degree of OR-PAM modality is calculated to be ~23 μm. Also, the sampling rate of the DAQ card was set at 100 MHz corresponding to a z axis spacing is 15μm. Z axis spacing is calculated by myltiplying the time interval between the acquisition of two sequential points which is (1/100MHz), 10nsec with the speed of sound(1500m/s ) . Finally, the time required for a three dimensional volume reconstruction of 200x200x400 voxels was around twelve minutes.

## *3.2 Samples and Procedure*

CLs are transparent to both available wavelengths, 1064nm and 532nm, thus colored lenses were used for the measurements. The method was applied successfully in semi rigid contact lenses and in three different categories of soft Cls were depicted, cosmetically tinted lenses, fully colored lenses through their volume and superficially colored lenses. The size of all the images is 13mm x 200 points.

**A. Cosmetic soft contact lenses**

Cosmetic Cls are tinted lenses which permit wearers change their iris color and correct refractive errors, providing a great variety in colors and patterns. For this study, ''Air Optics Colors' CLs' by Alcon were imaged. Alcon produces monthly soft Cls with nine different color options (figure 3.3 A) and the grain of printed dots as shown in figure 3.3 B.

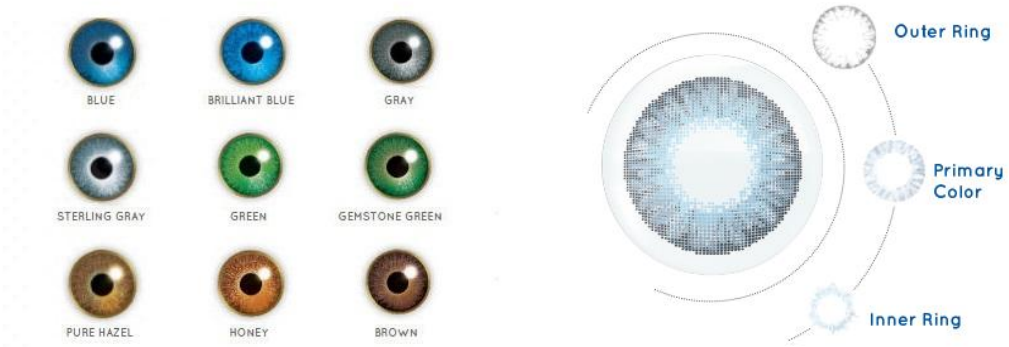


***Fig.3.3*** *: Air Optics Colors (Alcon) (A) Available colors, (B) Color allocation*

**B. Fully colored lenses**

In order to image the entire volume of the Cl, fully colored Cls ,IQ EYE 75% Brown, T58 Dark Brown and T74 75% Brown by David Thomas (Menicon Group) were measured. The lenses were fully colored except of the pupil part (figure 3.4).

***Fig. 3.4:*** *T74 75% Brown by David Thomas*

### C. Superficially colored lenses

- **Rigid gas permeable Cls**

We have employed rigid gas permeable (RGP) Cls (Menicon Z Comfort, Menicon) for our initial measurements, since they preserve their shape and do not present any flexure effect. Furthermore, both of the geometrical and optical parameters are provided independently by the manufacturer, allowing for a direct comparison between the nominal and experimental values.

- **Soft Contact lenses**

We have additionally used transparent soft Cls of several dioptric corrections, (Miru 1day Flat Pack by Menicon) to evaluate the system's performance for this lens category.

Cls were colored superficially using two different permanent markers. The anterior surface was colored black by a uniMarker (Mitsubishi) and the posterior was colored red by a STAEDLER (Lumocolor) permanent marker. During the time between the coating of the surfaces, the lens was hydrated by placing into distilled water for a minute, to prevent any deformation. The absorbance spectrum of the two markers show that the red marker presents a pick around 550nm, as well as, minimum absorption in infrared wavelengths, whereas the black one has a broad absorption range including the infrared region. Initially, the red colored posterior surface was measured using the 532 nm wavelength. Subsequently, without displacing the lens from its initial position, the black posterior surface was measured using the fundamental wavelength at 1064 nm.

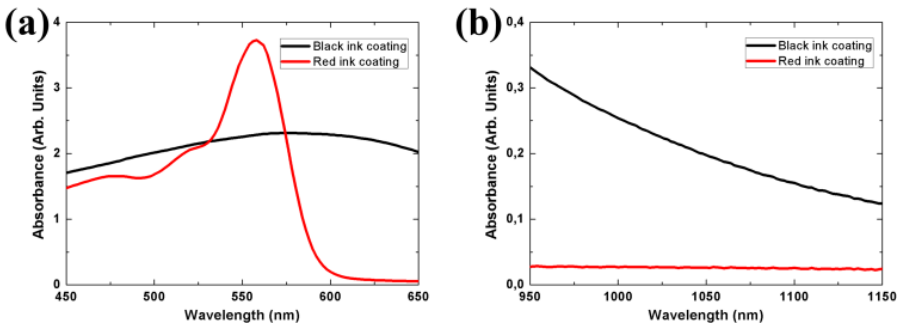


***Fig 3.5:*** Absorption spectra of black and red ink coatings for (a) 450-650 nm and (b) 950-1150 nm wavelength range

## *3.3 Processing of photoacoustic data*

A custom made automated algorithm was implemented in MATLAB programming environment to process the originally recorded 3d data representing the distribution of photoacoustic signals in space.. For the morphological inspection of the lens, the critical parameter is the time delay of the signal's maximum amplitude, rather than the maximum amplitude value itself. In other words, it is not the photoacoustic wave amplitude, but its respective position that reveals the Cl's local elevation. Thus, by mapping these positions, the initial matrix is transformed into a three dimensional elevation map depicting separately the two CL surfaces.

Following the determination of the maximum amplitude positions, the algorithm attempts to center the lens reconstruction by finding the median center coordinates (XY) of five fitted iso-altitude ellipses separated by 70 pixels. The result of this process is a centered elevation map of the original data. Then, using the formula for a second order polynomial of two variables

$$S(x,y) = ax^2 + by^2 + cxy + dx + ey + f \quad (3.3.1)$$

we fit the data points of the optical zone (6.5 mm diameter) to determine the coefficients of the polynomial equation. The $R^2$ value was higher than 0.99 showing high fitting quality. The mean curvature H of the surface is given by

$$H = \frac{1}{2}\frac{\left(1+\left(\frac{\partial S}{\partial x}\right)^2\right)\frac{\partial^2 S}{\partial y^2} - 2\frac{\partial S}{\partial x}\frac{\partial S}{\partial y}\frac{\partial^2 S}{\partial x \partial y} + \left(1+\left(\frac{\partial S}{\partial y}\right)^2\right)\frac{\partial^2 S}{\partial x^2}}{\left(1+\left(\frac{\partial S}{\partial x}\right)^2 + \left(\frac{\partial S}{\partial y}\right)^2\right)^{3/2}} \quad (3.3.2)$$

and the radius of curvature R(x,y) map is produced by taking the reciprocal of H as

$$R = \frac{1}{H} \quad . \quad (3.3.3)$$

Central lens thickness is calculated by subtracting the height coordinate of the centers of lens surfaces.

Finally, using the calculated radius of curvature maps for the two CL's surfaces R1 and R2 respectively, as well as, the respective central thickness value (CT), the dioptric power profile P(x,y) of the lens is calculated through the thick lens formula

$$P = (n-1)\left[\frac{1}{R_1} + \frac{1}{R_2} - \frac{(n-1)*CT}{n*R_1*R_2}\right] \quad (3.3.4)$$

were n is the CL's refractive index.

The refractive index used for the Miru lenses was n=1.409 and for Rigid gas permeable Cls was n=1.414.

## *3.4 Optical and acoustic distortion compensation for semi rigid Cls measurement*

Nevertheless, such high precision measurements of CLs parameters through the intrinsically hybrid PA effect, require a correction for optical and acoustic distortions originated from the different refractive and mechanical properties of the CL material compared to the surrounding immersion medium. As to the anterior surface measurement (Fig. 3a), the incoming excitation ray is bent according to Snell's law due to the refractive index difference between the CL (n2) and the distilled water (n1). If θ1 and θ2 are the angles of incidence and refraction respectively and θ3 is equal to θ1-θ2, it can be easily derived (see derivation at the end of this chapter) under a small angle approximation that

$$\Delta x = \frac{d\,\frac{x}{R}\left(1-\frac{n1}{n2}\right)}{1+\frac{n1}{n2}\left(\frac{x}{R}\right)^2} \qquad (3.4.1)$$

where Δx is the lateral deviation of the incident ray on the anterior surface level, x is the distance measured from the lens symmetry axis, R is the radius of curvature for the posterior surface and d is a vertical distance equal to Δx/tan(θ3). As a direct consequence, for the typical case where n2>n1, the induced refractive error results in a steeper anterior surface estimation due to the lateral distortion. To compensate for this deviation, we have multiplied the lateral dimensions of each voxel by a correction factor $M_A$= 1+(Δx/x) prior the final optical zone reconstruction, which for typical parameter values (x=3.25 mm, R=7.5 mm, d=0.15 mm, n1=1.33, n2=1.44) is calculated to be ~1.0013.

Regarding the posterior surface measurement (Fig. 3b), an axial distortion is generated during the propagation of the respective PA waves through the CL volume at a different speed (u2) compared to the immersion medium (u1). If we assume that the path length through the CL is equal to d and F is the relative distance between the ultrasonic detector and the anterior surface of the lens, a path-weighted average

ultrasonic speed $\bar{u}$ will be given by the expression $\bar{u}$=[d/(F+d)]*u2+[F/(F+d)]*u1. For approximate values of the involved parameters (d=0.15 mm, F=30 mm, u1=1480 m/s, u2=2500 m/s), $\bar{u}$ is estimated to be around 1485 m/s. Consequently, a posterior surface correction factor $M_P = \bar{u}/u1$ is introduced as a multiplying constant in the axial voxel size, with a typical value ~1.0034. In this context, the posterior CL surface is adjusted for the acoustic propagation distortion, which if not compensated, tends to flatten the respective reconstruction.

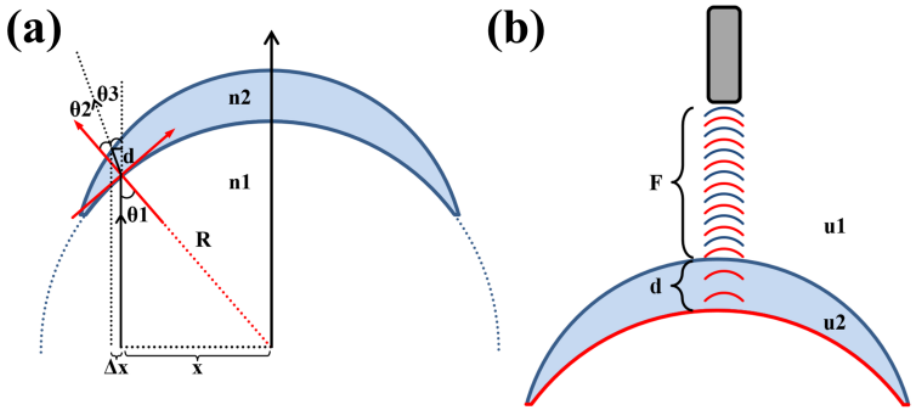


**Fig. 3.4.1** Optical and acoustic distortion errors affecting CL's surfaces reconstruction. (a) The refractive index mismatch between the lens material (n2) and the surrounding medium (n1) bends the incoming rays to introduce a lateral error Δx during the anterior surface measurement. (b) The transmission of photoacoustic waves through the lens material at speed u2 generates an axial distortion when measuring the posterior surface of the lens (red color).

Derivation of equation 3.4.1

The formulas above fot the Anterior surface refractive error correction is the result of the following analysis including Snell's law and simple geometrical aproximations

According to Snell's law: $n1\sin\theta1 = n2\sin\theta2$

Geometry indicates that the sine of angles θ1 and θ2 are given by:

$$\sin\theta1 = \frac{x}{R} \qquad \sin\theta2 = \frac{n1}{n2}\frac{x}{R}$$

Furthermore, $\Delta x = d\tan(\theta3) = d\tan(\theta1-\theta2)$

or $$\Delta x = d\frac{\tan(\theta1)-\tan(\theta2)}{1+\tan(\theta1)\tan(\theta2)}$$

Under a small angle approximation sinθ≈tanθ, therefore

$$\tan\theta 1 \approx \frac{x}{R} \qquad \tan\theta 2 \approx \frac{n1}{n2}\frac{x}{R}$$

By direct substitution of the expressions above, Δx is finally given by

$$\Delta x = \frac{d\,\frac{x}{R}\left(1-\frac{n1}{n2}\right)}{1+\frac{n1}{n2}\left(\frac{x}{R}\right)^2}$$

Q.E.D.

## *3.5 Errors of measurements*

- ***Lateral error***

The probable error is equal to half of the pixel size. Thus, the lateral error arising from pixel size (x,y) dimensions, which is 67.25 μm has a typical value of:

$$\Delta x = \Delta y = \frac{67.25}{2}\mu m = 33.6\mu m$$

- ***Axial error***

The axial error is ultimately limited by the ultrasonic transducer's detection bandwidth (Δf). A good approximation of the achieved axial resolution is the half of the typically detected wavelength:

$$\Delta z = \frac{u_s}{2\Delta f}$$

where $u_s$ is the speed of sound in the medium.

For our 100% relative bandwidth 20MHz detector

$$\Delta z = \frac{1500}{2\cdot 20\cdot 10^6} = 37.5\mu m$$

- ***Error of radius of curvature ΔR***

Error of radius of curvature $R = \sqrt{x^2 + y^2 + z^2}$ :

$$\Delta R \approx \pm\left[(\Delta x)^2 + (\Delta y)^2 + (\Delta z)^2\right]^{1/2}$$ typical error

$$\Delta R \approx \pm\left[\left(\frac{67.25}{2}\right)^2 + \left(\frac{67.25}{2}\right)^2 + (37.5)^2\right]^{1/2} = \pm(2261.28+1406)^{1/2} = \pm 60.55\mu m$$

$\Delta R \approx \pm$ 60.55μm or $\Delta R \approx \pm$ 0.061mm

- **Dioptric power error ΔP**

The dioptric power of each surface is calculated by the equation

$P_s = \frac{n-1}{R}$, therefore

$$\frac{dP_s}{dR} = -\frac{(n-1)}{R^2} \Rightarrow dP_s = -(n-1)\frac{dR}{R^2}$$

when ΔR<<R $\rightarrow \Delta R = dR$, $\rightarrow \Delta P_s = dP_S$ and $\Delta P_S = \pm(n-1)\frac{\Delta R}{R^2}$

Assuming that the total lens power D is the sum of the powers of the two surfaces $P_S(A)$, $P_S(B)$

$$\Delta P = \pm\left[(\Delta P_S(A))^2 + (\Delta P_S(B))^2\right]^{1/2}$$

For example, for a Cls with n=1.413, ΔR=0.061mm and R=8mm

$\Delta P_S = -0.26458D$

if $\Delta P_S(A) = \Delta P_S(B) = 0.26458D$

$\Delta P = \pm 0.374484D$

## *References*

Tserevelakis, G.J., Soliman, D., Omar, M., Ntziachristos, V. Hybrid multiphoton and optoacoustic microscope (2014) Optics Letters, 39 (7), pp. 1819-1822

# *Chapter 4: Experimental results*

To demonstrate the capabilities of photoacoustic methodology on the quality evaluation and geometrical/optical parameters evaluation of CLs, three categories of lenses were employed: a) cosmetic or homogeneously tinted soft lenses, b) semi-rigid contact lenses, and c) soft CLs. The CLs belonging in the first category were exclusively used for qualitative inspection, whereas the CLs of the second and third category were manually tinted and measured, in order to extract the quantitative data of interest.

## *4.1 Cosmetic soft contact lenses*

Regarding the color lenses, all the different colors presented in figure 3.3 could be imaged due to the high optical absorption of the pigments. It was observed that the brown shades would generally provide the strongest photoacoustic responses, in contrast to the blue shades which presented significantly lower signals. Figure 4.1 (a) shows the three layers of the grain of printed dots for Alcon color lenses as provided by the manufacturer, whereas Figure 4.1 (b) depicts a respective typical photoacoustic imaging reconstruction at different views. The obvious resemblance between the two figures, demonstrates the accuracy of the photoacoustic imaging approach as to the visualization of the tint pattern in color CLs.

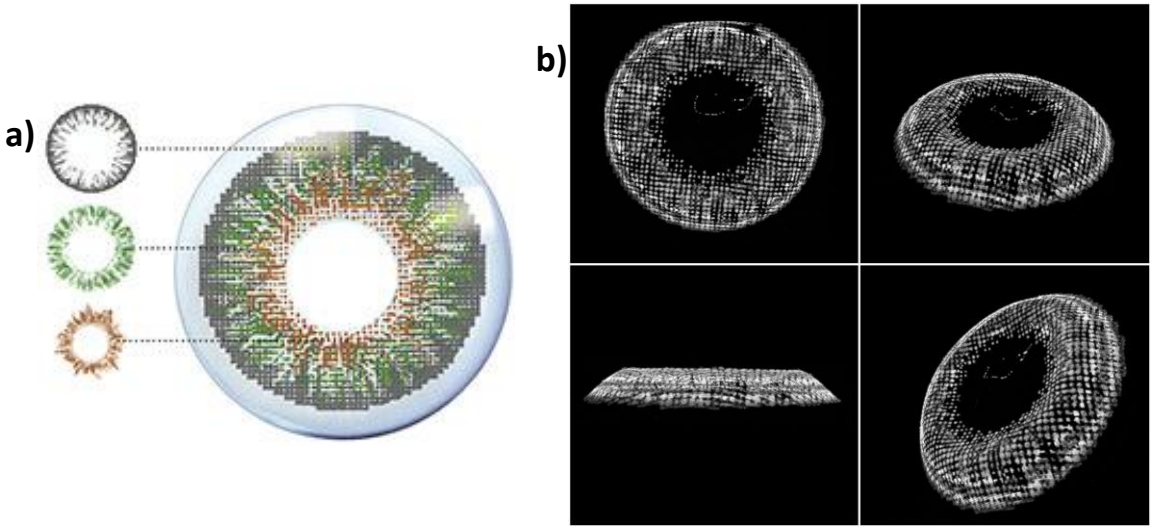


***Fig.4.1 :*** *(a) Grain of printed dots at Alcon color lenses. (b) Different views of a Brown Alcon color lens*

## *4.2 Homogeneously tinted lenses*

Fully colored lenses were used in order to image the entire volume of the Cl. Nevertheless, due to the high optical absorption of the color agent, the photoacoustic effect could not take place at depths more than a few μm within the CL. In this manner, the significant attenuation of the irradiation at the posterior surface, didn't allow for the photoacoustic excitation of the whole CL's volume. As a result, only the posterior surface of the lens was depicted.

Images in Figure 4.3 (A and B) show the posterior surface of two Cls colored uniformly through their volume except of the iris part. Lens A is a plano lens (P = 0D), while B has a positive dioptric power of P=+22.5 D, presenting an increased central thickness. The difference between the lens fitting for these cases can be seen in image C, which shows a central cross section of the two lenses. Lens B appears more curved than lens A as expected, due to the high difference in their dioptric powers. The outline of higher intensity is the posterior surface of the lens, while the second one is a reflection signal arising from the hemispherical base of the tank. Furthermore, it can easily be observed that lens B presents different radius of curvature at both its optical zone and periphery.

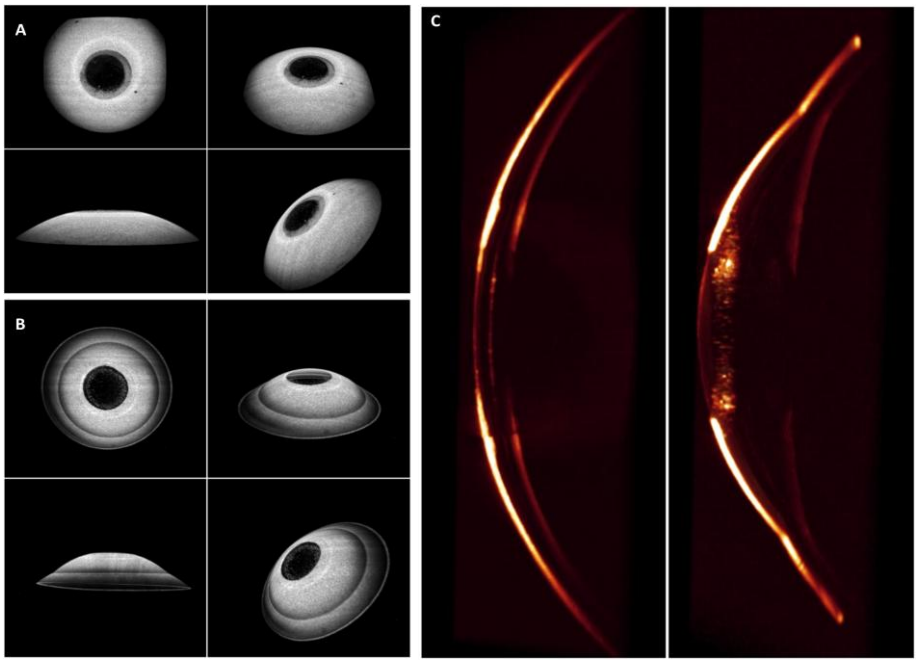


***Fig. 4.2:*** *(A) Plano (B) +22.5D (C) section of lens A and B respectively*

Additional details of the lens surfaces are shown at the volume rendering MIP image of lens B at figure 4.3. The tint lines are clearly distinguished at the posterior surface.

Moreover, similarly to image C, we can visualize the optical zone diameter and the different radius of curvature between the optical zone and the periphery of the Cl.

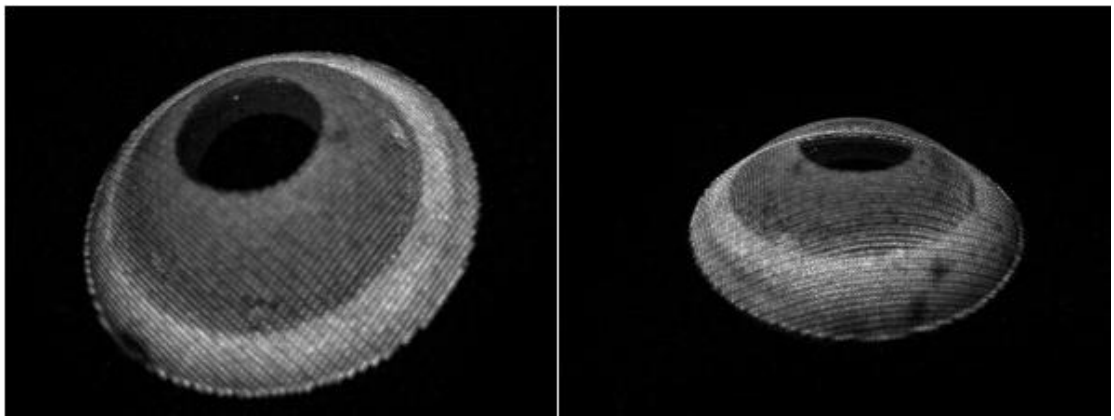

***Fig. 4.3**: MIP of T74 Brown (Menicon), Power:+22.5D*

## *4.3 System calibration prior measurements*

As a first step, the system was calibrated using an optically transparent hemispherical phantom of known geometrical properties. The calibration process is essential for improving the reconstruction accuracy due to the relative uncertainty regarding the exact ultrasonic speed in distilled water (~1485 m/s), as well as, the possible translational motion errors during the mechanical raster scanning.

Figure 4.6(a) shows the elevation map as reconstructed from the original photoacoustic data for the surface of the hemispherical phantom. On the contrary, Figure 4.6(b) constitutes the altitude map based on the second order polynomial surface fitting of a region corresponding to the typical optical zone of a CL (6.5 mm diameter). The resemblance of these two maps reflects the high fitting quality which is also apparent in the $R^2$ value. Figure 4.6(c) shows the radius of curvature map of the CL surface, through which we can further calculate the dioptric power distribution across the lens (Figure 4.6(d)).

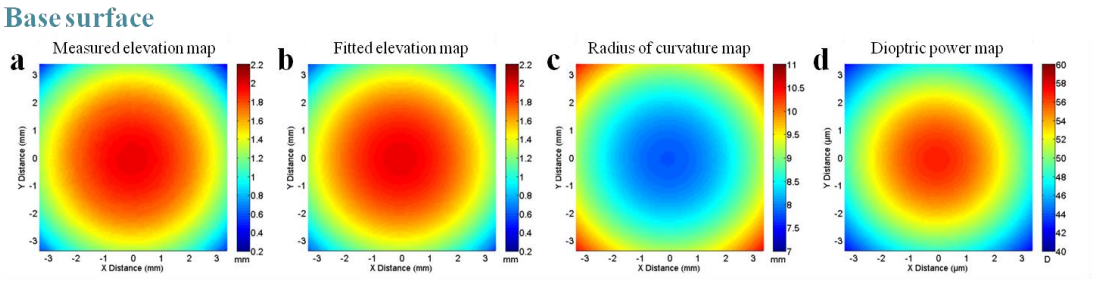


| | $R_V$ (±0.06mm) | $P_V$(D) | $\Delta P_V$(D) | $R^2$ |
|---|---|---|---|---|
| Base R=7.8mm | 7.80 | 56.76 | 0.44 | 0.99932 |

***Fig. 4.6:*** *Topographical map of the phantom surface of known curvature R=7.8 mm*

## *4.4 Surface measurements of double coated rigid gas permeable (RGP) CLs*

Following the end of the calibration, we proceeded to the surface measurements of three double coated rigid gas permeable (RGP) CLs. The generated data demonstrated the capability of geometrical and optical inspection of a Cl, by visualizing sequentially both of the CL surfaces.

As an example of our measurements, we present the generated maps for a -3.00 D CL having a posterior radius of curvature at 7.75 mm. Figure 4.7(a) shows the measured elevation map for the optical zone region (~6.5 mm diameter) of the anterior surface whereas Figure 4.7(b) shows the respective 2nd order polynomial fitting reconstruction ($R^2$=0.998) having the typical form S(x,y)= Ax2+By2+Cxy+Dx+Ey+F. The radius of curvature map R(x,y) depicted in Fig. 4.7(c) was subsequently calculated as the reciprocal of the mean curvature H for the fitted surface S.

In this manner, the radius of curvature R1 at the center of the CL was found to be 8.25±0.06 mm. The estimated typical measurement error ΔR for R1 calculation resulted from the combined contributions of the characteristic distance uncertainties in the lateral (~32.5 μm) and axial (~37 μm) dimensions. The dioptric power map P(x,y) of the anterior CL surface (Fig. 4.7(d)) was then directly determined through the common expression $P(x,y)=10^3(n-1)/R(x,y)$, where n=1.443 as provided by the lens manufacturer. Thus, a dioptric power P1=53.70±0.39 D was calculated at the center of the lens, whereas the respective typical error was estimated by the equation $\Delta P=\pm 10^3(n-1)\Delta R/R2$.

In an analogous procedure, similar maps were generated for the posterior CL surface as explicitly shown in Fig. 4.7e-h. Following the polynomial fitting ($R^2$=0.999), the radius of curvature R2 at the lens center was determined to be 7.75±0.06 mm, which is identical to the BC value provided by the manufacturer. Furthermore, the dioptric power P2 was estimated at -57.16±0.44 D, whereas the CL central thickness d resulted from the subtraction of the maximum elevation values for the two fitted surfaces (d=0.18±0.04 mm, manufacturer's given value: 0.17 mm). The total refractive power P of the lens P, was calculated using Gullstrand's formula $P=P1+P2-10^{-3}P1*P2*(d/n)$ at -3.08±0.59 D, assuming that the typical measurement error arises predominantly from the combined uncertainties in P1 and P2. The estimated refractive power was very close to its nominal value (-3.00 D), confirming thus the high reliability of the proposed CL characterization technique.

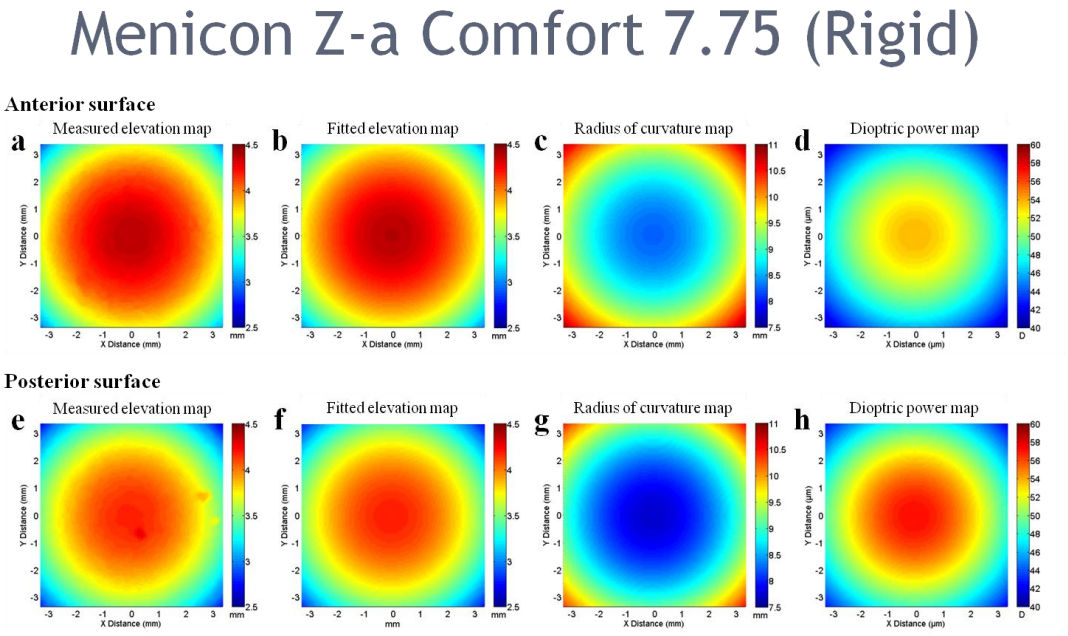


***Fig. 4.7:*** Surface measurements of a double coated Menicon Z-a Comfort R=7.75mm

Finally, the table shown in Figure 4.8, summarizes the obtained results for the three measured semi-rigid CLs.

| Contact Lens | Surface | $R_v$ (±0.06mm) | $P_v$(D) | $\Delta P_v$(D) | H(µm) | $R^2$ | Thickness (±0.038mm) | Power (D) | ΔP |
|---|---|---|---|---|---|---|---|---|---|
| Menicon z-a (P=-3.00 R=7.40mm) | Anterior | 7.8679 | 56.3046 | 0.42937 | 3022.74 | 0.99902 | 0.169 | -2.88 | 0.64 |
| | Posterior | 7.4354 | 59.5802 | 0.48079 | 2840.04 | 0.99904 | | | |
| Menicon z-a (P=-3.00 R=7.75mm) | Anterior | 8.2472 | 53.7154 | 0.39079 | 4379.15 | 0.99835 | 0.176 | -3.09 | 0.59 |
| | Posterior | 7.7473 | 57.1813 | 0.44285 | 4182.36 | 0.99921 | | | |
| Menicon z-a (P=-3.00 R=8.30mm) | Anterior | 8.9407 | 49.5487 | 0.33252 | 2645.20 | 0.99903 | 0.157 | -2.50 | 0.50 |
| | Posterior | 8.4658 | 52.3282 | 0.37087 | 2475.81 | 0.99817 | | | |

***Fig. 4.8:*** Surface measurements of three double coated rigid gas permeable (RGP) CLs.

## *4.5: Surface measurements of double coated soft CLs*

Six transparent lenses with different dioptric power (-10, -6, -4, -3, -0.75, +3D) were colored superficially and measured using dual wavelength excitation (532 and 1064 nm). The reconstruction of both, anterior and posterior, surfaces of the lens was achieved following the procedure described in *Chapter 3.2 C,* for the superficial coloring of transparent Cls. Two typical photoacoustic images of the anterior and posterior surfaces of such a colored lens are given in Figure 4.9, For this imaging sessions, the anterior surface was colored with black ink (Fig. 4.9(a)), whereas the posterior surface was colored with red ink (Fig. 4.9(b)).

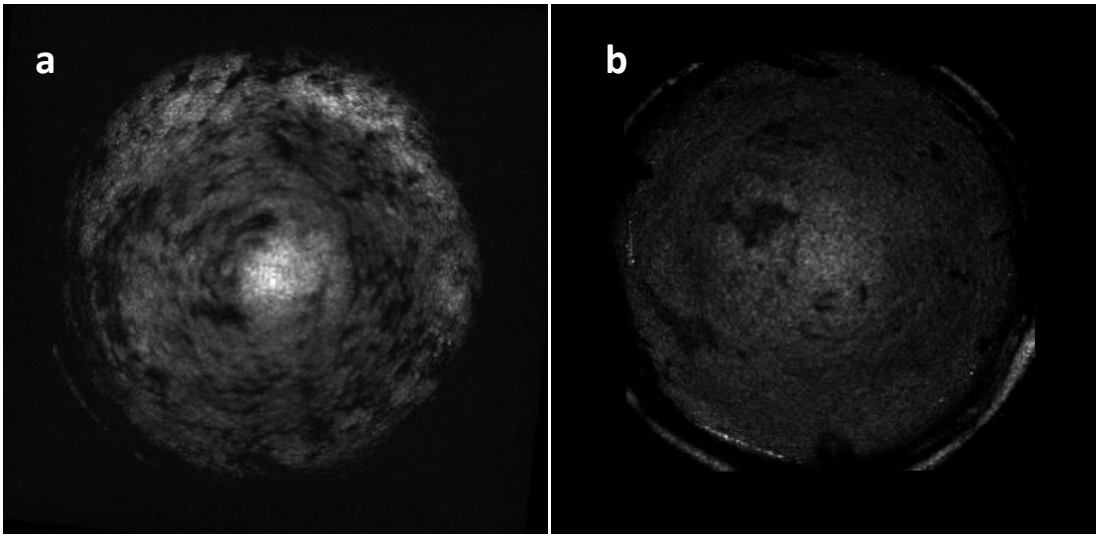


***Fig.4.9*** *Photoacoustic images of anterior (a) and posterior (b) surfaces of Miru flat pack lens, +3.00 D after superficial coloration.*

The quantitative results following the processing of the photoacoustic data are shown in the table of Figure 4.10.

| Contact Lens | Surface | $R_v$ (±0.06mm) | $P_v$(D) | $\Delta P_v$(D) | H(μm) | $R^2$ | Thickness (±0.038mm) | Power (D) | ΔP |
|---|---|---|---|---|---|---|---|---|---|
| Miru +4.00D | Anterior | 7.8429 | 52.1491 | 0.39895 | 5684.11 | 0.99632 | 0.180 | 3.60 | 0.53 |
| | Posterior | 8.3674 | 48.8801 | 0.3505 | 5503.27 | 0.99749 | | | |
| Miru +3.00D | Anterior | 8.2307 | 49.692 | 0.36224 | 5626.87 | 0.99758 | 0.241 | 2.27 | 0.49 |
| | Posterior | 8.5516 | 47.8271 | 0.33556 | 5385.41 | 0.99706 | | | |
| Miru -10.00D | Anterior | 12.4922 | 32.7403 | 0.15725 | 5374.62 | 0.99002 | 0.124 | -9.53 | 0.31 |
| | Posterior | 9.6486 | 42.3897 | 0.2636 | 5250.25 | 0.99178 | | | |
| Miru -6.00D | Anterior | 10.3649 | 39.4603 | 0.22843 | 5739.38 | 0.99225 | 0.162 | -5.07 | 0.37 |
| | Posterior | 9.1434 | 44.7316 | 0.29353 | 5577.86 | 0.99422 | | | |
| Miru -3.00D | Anterior | 9.4274 | 43.3844 | 0.27612 | 5758.78 | 0.99704 | 0.141 | -3.18 | 0.42 |
| | Posterior | 8.7456 | 46.7663 | 5617.39 | 5617.39 | 0.9969 | | | |
| Miru -0.75D | Anterior | 9.5478 | 42.8369 | 0.26919 | 5375.45 | 0.99281 | 0.178 | -1.40 | 0.4 |
| | Posterior | 9.1962 | 44.4749 | 0.29017 | 5197.79 | 0.99291 | | | |

***Fig. 4.10*** Surface measurements of six double coated soft CLs

As an example, we provide the generated maps for a Cl with P= -3.00 D (Figure 4.11); the first row includes the data for the anterior surface whereas the second row the respective data for the posterior surface. As expected, the dioptric power of the posterior surface is higher than the power of the anterior surface. Regarding the radius of curvature maps, the posterior surface appears to be more curved, revealing the negative power of the CL.

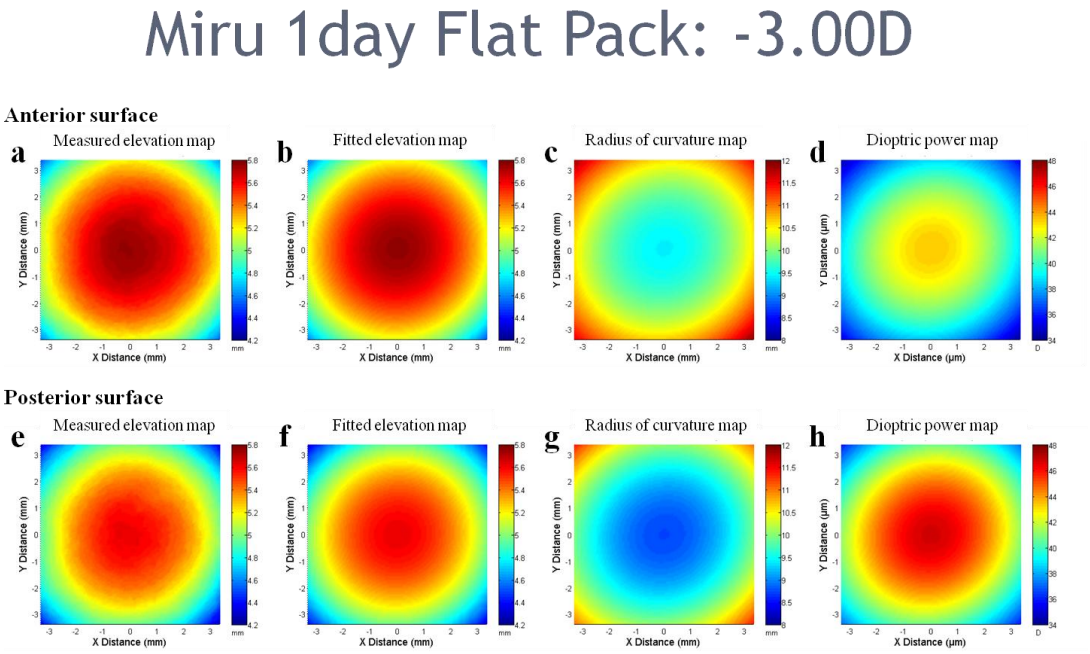


***Fig. 4.11*** *Surface measurements of a Miru 1day flat Pack lens: -3.00D.*

Looking at the topographic maps of a lens of positive dioptric power as the CL of Figure 4.12, with P=+3.00 D, we observe that in this case, the dioptric power of the posterior surface is higher than the power of the anterior and the curvature of the posterior surface appears to be smaller than the anterior.

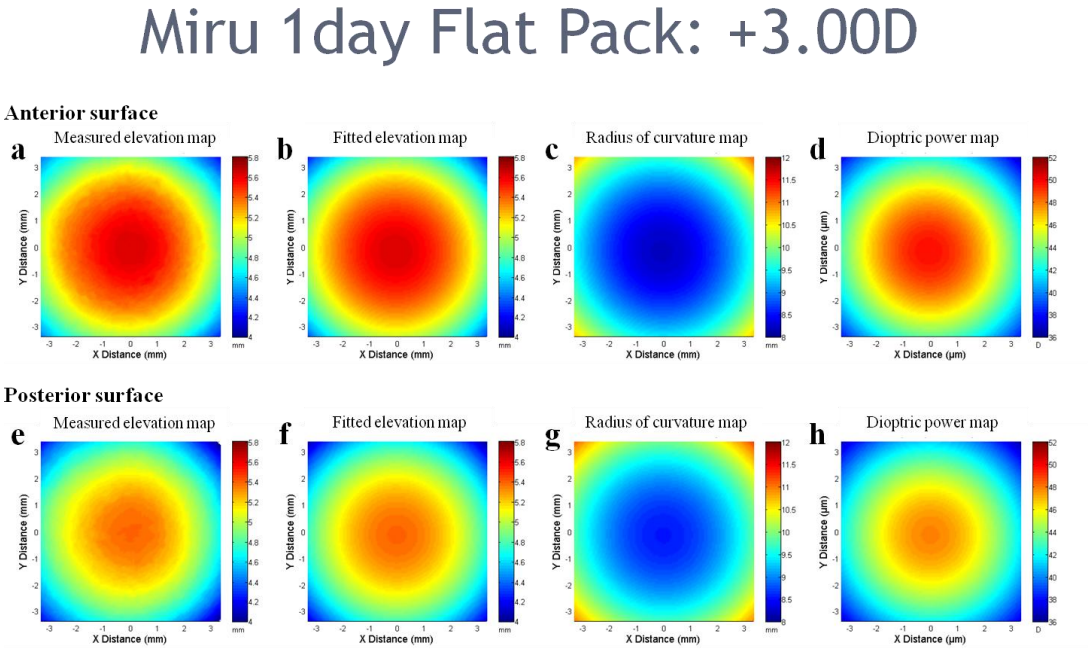


***Fig. 4.12*** *Surface measurements of a Miru 1day flat Pack lens: +3.00D.*

# *Chapter 5: Discussion and conclusions*

In this thesis, we have demonstrated photoacoustic microscopy as a metrology method for the optical characterization and quality control of CLs. The method is capable of measuring the elevation maps of both CL surfaces during two subsequent imaging sessions and extracts important optical parameters such as CL thickness, curvatures and dioptric power. The precision of the measurements are ultimately limited both by the laser beam diffraction (lateral resolution) and the acoustic detection bandwidth of the employed detector (axial resolution). Nevertheless, for the purpose of this work, the applied data undersampling of the XY plane (65 μm), resulted in a satisfactory determination of the geometrical properties of interest at an acceptable data acquisition time. The measurement errors could be potentially minimized through the use of a higher numerical aperture objective lens for the improvement of the lateral detail resolving degree, in combination to an adequate data sampling that would fulfill Nyquist's criterion. Under such conditions, the lateral resolution of the system could be better than 20 μm, which constitutes a significant upgrade as to the precise measurement of a CL's optical properties. Regarding the axial resolution of the proposed methodology, this could be further enhanced through the use of a broadband ultrasonic transducer being able to detect efficiently a larger portion of the emitted acoustic energy. For example, by employing a sufficiently long working distance detector with a central frequency of 80 MHz and a relative detection bandwidth of 125%, an axial resolution of up to 7 μm can be achieved. Therefore, the paired lateral and axial resolution improvements could finally lead to the calculation of the total CL's correction with an uncertainty of less than 0.25 D, a value which constitutes the increment step as to the nominal dioptric power of commercial CLs.

We have observed that while the measurements of the semi-rigid CLs were in fact quite accurate, and the obtained data matched the manufacturer's values, the respective geometrical and optical parameters estimation as to the soft CLs, was characterized by larger errors, at least concerning the total dioptric power of the lens. This extra difficulty in determining the properties of soft CLs compared to the semi-rigid ones was actually expected because of several technical issues such as: a) the incorrect CL's fitting on the hemispherical resin base, b) the poor quality of the manually applied coatings on hydrogel-silicone surfaces, c) the induced CL's deformation during the coating procedure, and d) the uncompensated optical distortions originating from the base. In addition to the latter reasons, the deviation of some of our measurements in comparison to the nominal values can be attributed to

the fact that during the design of a CL, the manufacturers usually take into account the tear lens effect which can alter the total power of the CL when applied on the eye. More specifically, when the resulting curvature of the posterior Cl's surface is lower than the respective curvature of the user's cornea, a minus tear lens is formed between the two surfaces, influencing the effective dioptric correction. On the contrary, when the curvature of the CL is higher than the curvature of the cornea, the generated plus tear lens increases the CL's power towards positive values. Therefore, the compensation for this effect can lead to actual dioptric powers which are slightly different (~0.25 D) than the respective nominal ones.

We strongly believe that the majority of the described problems could be effectively minimized, following the use of a base having similar geometrical and optical properties with an average corneal surface (e.g. asphericity). This much more realistic scenario would allow the optimization of the measurement process, increasing thus the accuracy of the obtained information. In addition, the tinting procedure has to be performed in a more reliable and sophisticated manner which will ensure that it will not affect the original geometrical and refractive properties of the lens. Finally, in the case of soft CLs measurement, the data processing can be further upgraded in order to predict and compensate for optical distortions due to the base, as well as, the tear lens effects during the application of the lens.

In conclusion, we have presented a novel universal methodology based on the PA effect for the precise optical characterization and 3D imaging of both semi-rigid and soft contact lenses. The implementation simplicity, as well as, the robustness of the proposed technique compared to interferometric measurements, render it suitable for a broad industrial application regarding CL quality inspection and optimization. Furthermore, the total cost of the setup can be drastically reduced by adopting a frequency domain PA microscopy approach, incorporating low-budget CW laser sources at multiple excitation lines. Finally, data analysis can also be extended in the direction of higher order optical aberrations measurement, the study of soft CL fitting/flexure on the eye and the investigation of more complex profiles such as the multifocal CLs used in presbyopia correction.